6G BRAINS Deliverable D3.2

Specifications and Upgrade of Multiband Channel Sounder for Quad-Band Measurements at Sub-6 GHz + mmWave + THz + OWC in Industry Scenarios

Editor:	Bastien BECHADERGUE, Oledcomm
Deliverable nature:	Report (R)
Dissemination level: (Confidentiality)	Public (PU)
Contractual delivery date:	June 30, 2022 (M18)
Actual delivery date:	July 04, 2022
Suggested readers:	Consortium members, reviewers, researchers
Version:	1.0
Total number of pages:	58
Keywords:	Channel sounder, propagation measurement, THz, sub-6GHz, mmWave, optical wireless communications, Industry 4.0

Abstract

The present document details the architecture, implementation and calibration of a quad-band channel sounder operating in the sub-6 GHz (center frequency of 6.75 GHz), mmWave (center frequency of 74.25 GHz), sub-THz (center frequency of 186.75 GHz) and optical (peak wavelength of 940 nm) domains. This channel sounder is composed of two independent sounders – one for the optical band and the other for the sub- 6 GHz, mmWave and sub-THz bands – that are assembled in a single movable unit that can easily be deployed in industrial environments for multi-band channel measurements. Such measurements are envisioned in various setups that are here presented and will be later used to validate and calibrate the ray-tracing channel model developed in a previous report from point cloud data acquired with 3D laser measurements.

Disclaimer

This document contains material, which is the copyright of certain 6G BRAINS consortium parties, and may not be reproduced or copied without permission.

In case of Public (PU):

All 6G BRAINS consortium parties have agreed to full publication of this document.

In case of Restricted to Programme (PP):

All 6G BRAINS consortium parties have agreed to make this document available on request to other framework programme participants.

In case of Restricted to Group (RE):

All 6G BRAINS consortium parties have agreed to full publication of this document. However this document is written for being used by <organisation / other project / company etc.> as <a contribution to standardisation / material for consideration in product development etc.>.

In case of Consortium confidential (CO):

The information contained in this document is the proprietary confidential information of the 6G BRAINS consortium and may not be disclosed except in accordance with the consortium agreement.

The commercial use of any information contained in this document may require a license from the proprietor of that information.

Neither the 6G BRAINS consortium as a whole, nor a certain part of the 6G BRAINS consortium warrant that the information contained in this document is capable of use, nor that use of the information is free from risk, accepting no liability for loss or damage suffered by any person using this information.

The EC flag in this document is owned by the European Commission and the 5G PPP logo is owned by the 5G PPP initiative. The use of the EC flag and the 5G PPP logo reflects that 6G BRAINS receives funding from the European Commission, integrated in its 5G PPP initiative. Apart from this, the European Commission and the 5G PPP initiative have no responsibility for the content of this document.

The research leading to these results has received funding from the European Union Horizon 2020 Programme under grant agreement number 101017226 – *6G BRAINS – H2020-ICT-2020-2. The content of this document reflects only the author's view and the Commission is not responsible for any use that may be made of the information it contains.*

Impressum

[Full project title]	Bring Reinforcement-learning Into Radio Light Network for Massive Connections
[Short project title]	6G BRAINS
[Number and title of work-package]	WP3: 6G Physical Propagation Measurements and Modelling, from Microwave to THz and OWC
[Number and title of task]	T3.1: Multi-Band (MW + mmWave + THz + OWC) Channel Measurements in the Industrial Network Environments and Industrial Applications T3.2: Analysis of measurement data and elaboration of the differences in wave propagation T3.3: Common fused channel model for the industrial network environments and industrial
[Document title]	Specifications and upgrade of multiband channel sounder for quad-band measurements at sub-6 GHz + mmWave + THz + OWC in industry scenarios
[Editor: Name, company]	Bastien BECHADERGUE, Oledcomm
[Work-package leader: Name, company]	Diego DUPLEICH, Fraunhofer
[Estimation of PM spent on the Deliverable]	20 PM

Executive Summary

Future wireless communication systems rely on heterogeneous networks with the simultaneous utilization of sub-6 GHz, mmWave, sub-THz, and optical wireless communications (OWC) bands [6GB21]. The free blocks of spectrum available at mmWave, sub-THz and optical bands enable the implementation of high data rate wireless links with enhanced capacity, reliability, latency, and with an unprecedented level of accuracy and resolution in sensing applications. The 6G BRAINS project thus envisions the integration of such novel bands to support the development of ubiquitous smart wireless communications in industrial scenarios.

To that extent, the work carried out within WP3 aims at developing a single channel model which covers such a wide spectrum of frequency bands. Reliable channel models are indeed of exceptional importance for the design, performance evaluation, standardization, and deployment of the future sixth generation (6G) networks, and characterization of propagation at these frequencies is the initial step towards the development of these technologies.

The major objective driving the work of WP3 is to understand the similarities and differences in the propagation at these different frequencies to adjust the models we already have for sub-6 GHz, or to parametrize more suitable ones, such as ray-tracing (RT) models. More precisely, the final objective of WP3 is to develop a deterministic model based on RT for a specific industrial scenario and to then include stochastic elements to obtain an efficient fused multi-band channel model for various other industrial scenarios.

Whatever the modeling approach adopted, the relevance of the proposed model can only be evaluated by comparison with real world channel measurements, which can also be used for the model calibration. Channel sounders must be designed according to the measurement purposes and channel dimensions to be investigated. In particular, the geometrical properties of the multipath components must be resolved, i.e., their delay, direction of departure, direction of arrival and polarization. Moreover, due to the increased frequency, Doppler must be carefully considered in scenarios with high mobility. However, the measurements of such various parameters in the mmWave, sub-THz and OWC bands are still rudimentary, especially in industrial environments.

Consequently, there is still a lot of work to be done to better understand these communication channels. This is why the work of WP3 aims to develop a multi-band channel sounder that can be used to perform measurements in such environments.

The present document details the architecture, design and characterization of the fundamental elements of the multi-band (i.e., sub-6 GHz, mmWave, sub-THz, OWC) channel sounder developed in the framework of the 6G BRAINS project for the validation and calibration of the RT channel model proposed in D3.1 [6GB31].

This channel sounder is actually composed of two independent channel sounders integrated in the same equipment to perform channel measurements on all these four bands:

- The first channel sounder operates simultaneously on the sub-6 GHz (center frequency of 6.75 GHz), mmWave (center frequency of 74.25 GHz) and sub-THz (center frequency of 186.75 GHz) bands. For this purpose, a unified architecture has been developed: a single M-sequence excitation signal with a post-calibration bandwidth of 4 GHz is generated by an unique baseband, then different IF up/down converters allow transposition from/to the three frequency bands mentioned above. The transmitted

and received signals are then processed according to a specific process in order to extract the channel impulse response (CIR) and the spreads of the three channels of interest. This first channel sounder has been extensively tested in four scenarios to verify the calibration of the frequency response, the delay, the polarization and the start and end angle values it provides.

- The second channel sounder operates only in the optical band (peak wavelength of 940 nm) and consists of an analog OWC transceiver coupled to a signal processing platform. In transmission, the OWC transceiver is based on a single light source with variable directivity (half-power beam width of 45° or 10°) according to the needs, but respecting in all cases the eye safety standards. On the receiving side, four photodiodes coupled with focusing lenses are used to optimize the optical power collected and thus the quality of the received signal, allowing the developed OWC receiver to surpass existing photoreceptors on the market in terms of 'collection power'. The opto-electronic characterization of the OWC transceiver thus obtained shows that the modulation bandwidth at 3 dB and 6 dB are respectively 36 MHz and 47.5 MHz. The signal processing platform generates on its side a multi-sine signal with a bandwidth after calibration of 50 MHz, which once received after free space propagation is processed to extract the CIR and path loss of the optical propagation channel.

Both channel sounders are in practice assembled in a head with programmable orientation in order to perform tests in real environments. Some of the test environments envisaged for the continuation of the WP3 work are finally presented. The tests which will be carried out there will then be the subject of the deliverable D3.3.

List of Authors

Company	**Author**	**Contribution**
Fraunhofer	Diego Dupleich	Sections 1, 3, 4, and 5
Fraunhofer	Alexander Ebert	Sections 3 and 4
Fraunhofer	Leon Löser	Sections 3 and 4
Oledcomm	Bastien Béchadergue	Sections 1, 2 and 6, Executive Summary, Abstract and editing
Bosch	Alexander Artemenko	Section 5, review

Table of Contents

List of Figures and Tables

Abbreviations

5G	Fifth Generation (mobile/cellular networks)
5G PPP	5G Infrastructure Public Private Partnership
6G	Sixth Generation (mobile/cellular networks)
AGC	Automatic Gain Controller
APD	Avalanche Photodiode
AS	Azimuth Spread
BPF	Bandpass Filter
CAD	Computer Assisted Design
CIR	Channel Impulse Response
DC	Direct Current
DoA	Direction of Arrival
DoD	Direction of Departure
DR	Dynamic Range
DS	Delay Spread
ES	Elevation Spread
FFT	Fast Fourier Transform
FR	Frequency Response
FSPL	Free-Space Path-Loss
HPBW	Half-Power Beam Width
HRPE	High-Resolution Parameter Estimation
ICAS	Integrated Communication and Sensing
IF	Intermediate Frequency
IoT	Internet of Things
KPI	Key Performance Indicator
LED	Light Emitting Diode

LNA	Low Noise Amplifier
LO	Local Oscillator
LOS	Line-of-Sight
M2M	Machine to Machine
MIMO	Multiple-Input Multiple Output
MLBS	Maximum-Length Binary Sequence
NIR	Near Infrared
NLOS	Non-Line-of-Sight
OFDM	Orthogonal Frequency-Division Multiplexing
OMT	Orthomode Transducer
OTA	Over-The-Air
OWC	Optical Wireless Communications
PA	Power Amplifier
PADP	Power Azimuth/Delay Profile
PAP	Power Azimuth Profile
PAPR	Peak-to-Average Power Ratio
PD	Photodiode
PDP	Power Delay Profile
PEP	Power Elevation Profile
PIN	Positive Intrinsic Negative
PLL	Phase Locked Loop
PN	Pseudo Noise
PRBS	Pseudo Random Binary Sequence
RF	Radio Frequency
RMS	Root Mean Square
RT	Ray-Tracing

RX	Receiver
Si	Silicon
SLAM	Simultaneous Localization and Mapping
SMA	SubMiniature Version A (Connector)
SNR	Signal-to-Noise Ratio
TIA	Transimpedance Amplifier
TX	Transmitter
USB	Universal Serial Bus
UWB	Ultra-Wideband
VNA	Vector Network Analyzer

1 Introduction

1.1 Context

Future wireless communication systems rely on heterogeneous networks with the simultaneous utilization of sub-6 GHz, mmWave, sub-THz, and optical wireless communications (OWC) bands [6GB21]. The free blocks of spectrum available at mmWave, sub-THz and optical bands enable the implementation of high data rate wireless links with enhanced capacity, reliability, latency, and with an unprecedented level of accuracy and resolution in sensing applications. The 6G BRAINS project thus envisions the integration of such novel bands to support the development of ubiquitous smart wireless communications in industrial scenarios.

To that extent, the work carried out within WP3 aims at developing a single channel model which covers such a wide spectrum of frequency bands. Reliable channel models are indeed of exceptional importance for the design, performance evaluation, standardization, and deployment of the future sixth generation (6G) networks, and characterization of propagation at these frequencies is the initial step towards the development of these technologies. Channel modeling also allow us to understand fundamental aspects and foresee possible issues and opportunities.

For example, from the radio frequency (RF) perspective, the increasing isotropical free space path loss with increasing frequency requires the utilization of high gain antennas. Hence, the spatial characteristics of the channel, i.e., direction of arrival (DoA) and direction of departure (DoD), become a critical parameter since the system must know where the gain of the antenna must be steered. In addition, high gain antennas also isolate multipath components in the spatial domain reducing fading [DIS17], and aspects such as polarization become more relevant [DFM14, DFV15, DMS20]. Therefore, accurate spatial and geometrical properties of the propagation must be studied and included in channel models in order then to better design and optimize antennas.

In addition to such practical motivations, the major objective driving the work of WP3 is to understand the similarities and differences in the propagation at such different frequencies to adjust the models we already have for sub-6 GHz, or to parametrize more suitable ones, such as ray-tracing (RT) models. As further explained in Section 1.3, the final objective of WP3 is actually to develop a deterministic model based on RT for a specific industrial scenario and to then include stochastic elements to obtain an efficient fused multi-band channel model for various other industrial scenarios.

The reasons for this choice are multiple. From a non-OWC perspective, since the spatial characteristic and geometrical properties of the environment are not as determinant at sub-6 GHz as at mmWave due to the low resolution in the different domains of the communication systems, pure stochastic models may indeed be suitable. However, the use of such models is challenging with massive multiple-input multiple-output (MIMO) applications, and practicably obsolete for mmWave and sub-THz. In addition, pure stochastic models do not offer the necessary conditions for testing integrated communication and sensing (ICAS), simultaneous localization and mapping (SLAM), and many other applications.

On the contrary, deterministic models such as RT offer the possibility to obtain accurate representations of the channel. However, RT modelling is site specific, and its accuracy depends on the level of details and modelling efforts. Therefore, the inclusion of deterministic components in stochastic models has gained relevance [MML11, MMM22].

On the OWC side, the same trends can be observed. Many channel models have been proposed since the first work of Gfeller and Bapst in 1979 [GB79] and can, as in the RF world, be divided into two main categories: deterministic models and stochastic models [AWZ18].

Stochastic models apply the laws of wave propagation to geometries of transmitters (TXs), scatterers and optical receivers (RXs) predefined according to certain probability distributions and not according to the real geometry of the environment studied [PBB97, JPN02]. They offer great flexibility while largely limiting the computation time, but at the cost of limited accuracy, especially in complex environments such as industrial environments where the probability of line-of-sight (LOS) blockage is non-negligible and where non-LOS (NLOS) or indirect paths can play a critical role in maintaining communication.

Deterministic models are based on a detailed description of the propagation environment under study, and allow the impulse response and thus the frequency response (FR) of the channel to be calculated accurately using simulations that are nevertheless intensive and therefore resource-intensive. Several approaches have been proposed for this purpose. For simple environments, the temporal model proposed by Barry *et al.* [BKK93] and then optimized by Carruthers and Kannan [CK02] is still the reference, but its execution time explodes rapidly with the considered reflection order and spatial resolution.

Schulze has thus proposed a physically equivalent frequency model that is much faster to run [SCH16], but not applicable alone to complex environments. To overcome this limitation, this model has very recently been coupled to LIDAR point clouds in order to model the OWC communication channel in a real-world meeting room. In parallel, several works based on RT and using for example the commercial software Zemax© have been published [MU15], but the simulation time is here again exponential with the environment complexity.

This is why some studies have recently tried with success to mix deterministic and stochastic approaches, or at least to include geometrical elements in stochastic model and conversely. For example, in [ZWH22], a geometry-based stochastic model is proposed as a potential reference model for the standardization of OWC within the 6G framework. Other examples can be found in [CZK14], where a Combined Deterministic and Modified Monte Carlo method is adopted, or in [BCA17] where a Markov Chain Monte Carlo approach is preferred.

Whatever the modeling approach adopted, the relevance of the proposed model can only be evaluated by comparison with real world channel measurements, which can also be used for the model calibration. Unfortunately, channel measurements are usually time consuming and site as well as conditions specific. It is very important not only to carefully design the measurement scenario, but also to consider the characteristics of the measurement equipment – i.e. the channel sounder – to minimize its influence by means of calibration and verification. In that regard, there has been an increased interest from academy and industry in the metrology of measurements and communications at mmWave [IEE22] and sub-THz [HBK19].

Channel sounders must be designed according to the measurement purposes and channel dimensions to be investigated. With the previously highlighted propagation characteristics at mmWave and sub-THz, the geometrical properties of the multipath components must be resolved, i.e. their delay, DoD, DoA and polarization. Moreover, due to the increased frequency, Doppler must be carefully considered in scenarios with high mobility.

While these aspects have been extensively investigated from measurements and high-resolution parameter estimation (HRPE) applying MIMO channel sounders at sub-6 GHz, the state of the art in sounding at mmWave and sub-THz is still rudimentary. There are very few examples still on development of antenna arrays with the capability of high resolution at these frequencies. Therefore, the obtainable resolution in the measurements is still mostly based on the hardware capabilities (bandwidth for the delay, antenna directivity for DoD and DoA, sampling rate for Doppler) and the analysis of the measurement results are based on the identification of peaks in the different dimensions applying fast Fourier transform (FFT) based analysis [DSA22].

OWC channel measurement campaigns are not so common either, and mostly focused on indoor environments such as offices or corridors [HYK94, MK96, CZH15], at the notable exception of [BSH18], where the communication channels between several OWC TXs and RXs installed in a manufacturing cell have been measured.

Consequently, there is still a lot of work to be done to better understand the communication channels in industrial environments, whether in the sub-6GHz, mmWave, sub-THz or OWC bands. This is why the work of WP3 aims to develop a multi-band channel sounder that can be used to perform measurements in such environments, which will then be compared with the RT model already proposed.

1.2 Objectives and Structure of This Document

The objectives of this deliverable can be summarized as follows:

- Detail the architecture and characterization of the OWC channel sounder developed for the near infrared (NIR) band (Section 2),
- Detail the architecture, design and calibration of the multiband RF ultra-wideband (UWB) dual-polarized channel sounder developed for the sub-6 GHz, mmWave and sub-THz bands (Section 3),
- Details the architecture and calibration of the assembled channel sounder for quad band RF and OWC (Section 4).
- Introduce the test scenarios where this assembled channel sounder will be deployed and used in future works (Section 5).

1.3 Relation to Other Deliverables Within the WP3

The work of WP3 should lead to the production of five deliverables, as illustrated in Figure 1:

- Deliverable D3.1, which was published in [6GB31], presents the RT model used as channel model in 6G BRAINS, [6GB22]. This model was obtained from point cloud data measurements.
- As previously mentioned, the present document (i.e. D3.2, highlighted in dark green in Figure 1) is related to the design and characterization of the multi-band measurement equipment that will then be used for channel measurements.
- Deliverable D3.3 will detail the RF and OWC measurement campaigns carried out for RT calibration purposes with the channel sounder described here.

- Deliverable D3.4 will deal with the calibration and verification of the RT model, based on RF measurements. This step will be divided in:
    1) The calibration and verification of the computer assisted design (CAD) model by identifying differences between the geometrical properties obtained from the measured propagation paths and the geometry of the scenario,
    2) Then the calibration and verification of the electromagnetic properties of the materials assigned to the RT model, which will be made by comparing the amplitude levels of the different paths identified in the measurements.
    3) Finally, once the RT model will be verified and calibrated, stochastic components obtained from the measurements will be incorporated to the RT results to obtain the fused multi-band channel model for industrial scenarios.
- Deliverable D3.5 will finally address the results based on the integration of the waveforms under test into the simulations.

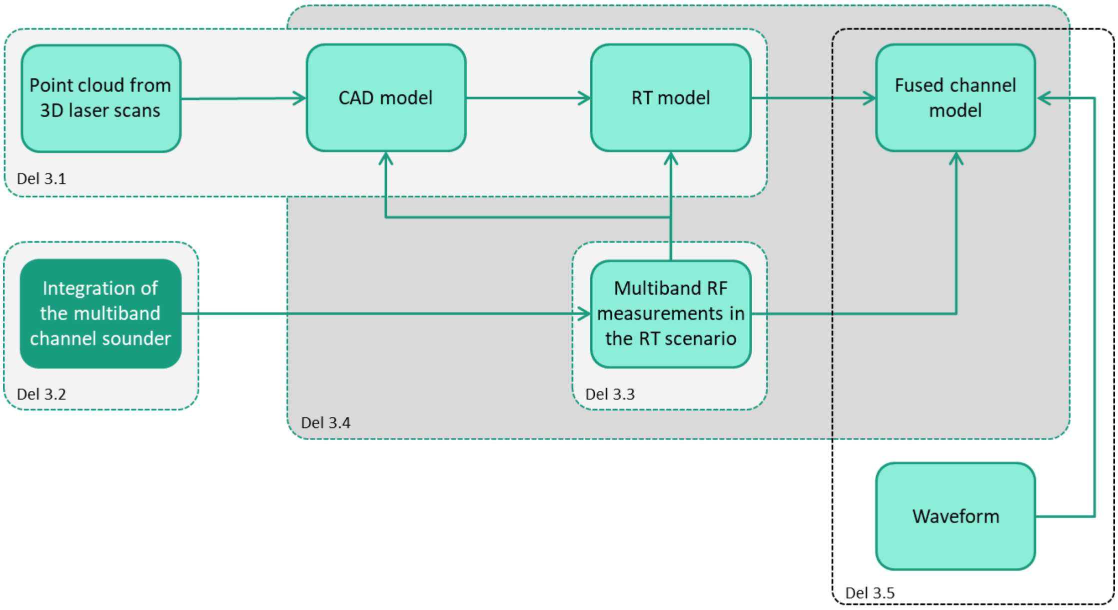

Figure 1 – Relation between workflow and deliverables within WP3.

2 OWC Channel Sounder

In this section, the design hypothesis and specifications of the OWC transceiver used for channel sounding are established after an analysis of the constraints imposed by the channel sounding method adopted in the 6G BRAINS project (i.e., frequency sweep) and by the main impairments caused by the optical propagation channel (Section 2.1). The architecture adopted to fulfill this specification is then detailed, with a particular focus on the characteristics of the optical TX and RX (Section 2.2). Finally, an opto-electronic characterization of the fabricated OWC transceiver is detailed (Section 2.3).

2.1 OWC Transceiver Specifications and Design Hypothesis

2.1.1 OWC Channel Sounding Principles

The role of the OWC transceiver integrated in the channel sounder is to transmit and receive a light signal allowing to estimate the response of the OWC communication channel. Within the framework of the 6G BRAINS project, the method adopted consists in estimating the FR of this channel by emitting a multi-sinus signal. This method is more extensively detailed in the Section 4.2 but produces results similar as that obtained when using a continuous frequency sweep, which explanation of the basic principles provides valuable insights to extract the specifications of our OWC transceiver.

In its most common version, the measurement of the FR of a channel using a frequency sweep is carried out using a vector network analyzer (VNA) on the output (i.e. port 1) of which is connected an OWC TX and on the input (i.e. port 2) of which is connected an OWC RX. The VNA supplies a sinewave on its port 1 whose frequency varies from a minimum value f_{min} to a maximum value f_{max}, and which drives the intensity of the light source of the OWC TX.

The optical signal thus emitted is, after propagation in free space, collected by the OWC RX and then transmitted to the port 2 so that the VNA can calculate in real time the parameter S_{12}. This parameter corresponds to the FR of the whole link, noted here $H_{link}(f)$ and defined by

$$H_{link}(f) = H_{Rx}(f)H(f)H_{Tx}(f) = H_{sys}(f)H(f), \tag{1}$$

with $H_{sys}(f) = H_{Rx}(f)H_{Rx}(f)$ and where $H_{Rx}(f), H(f)$ and $H_{Tx}(f)$ are respectively the FRs of the OWC TX, of the optical propagation channel and of the OWC RX [MHH19].

In other words, the FR obtained using the frequency sweep technique depends directly on the characteristics of the OWC transceiver, which must therefore be calibrated in order to correct the channel measurements made to extract the FR of the optical propagation channel $H(f)$ only.

To do this, the TX and RX must be placed at a minimum distance d_{ref} in order to limit the attenuation of the optical signal due to free space propagation while avoiding non-linear distortions. In this case, the FR obtained $H_{ref}(f)$ is such that

$$H_{ref}(f) = H_{sys}(f)H_d(f). \tag{2}$$

We can then estimate a normalized value $\widehat{H}(f)$ of the FR of the optical propagation channel using:

$$\hat{H}(f) = \frac{H_{link}(f)}{H_{ref}(f)}. \tag{3}$$

We can conclude from these first equations that the estimation of the FR of the optical propagation channel will be all the more reliable as the FRs of the measured and reference link $H_{link}(f)$ and $H_{ref}(f)$ will be stable, whatever the static geometrical configuration of the link. However, this geometrical configuration has a direct influence on the optical power collected by the photoreceptor, thus on the signal-to-noise ratio (SNR) of the input signal of the VNA and thus on the stability of the FR of the measured link, as we are now going to detail.

2.1.2 Key Parameters of the OWC Transceiver for Channel Sounding

Although incomplete, the LOS optical propagation channel model established in the OWC literature provides valuable insights into the critical points in the design of the OWC transceiver to optimize the SNR of the received signal. This model stipulates that the FR of the LOS optical channel $H_{LOS}(f)$ is such that [SCH16]

$$H_{LOS}(f) = \eta_{Rx,Tx}\, e^{-j2\pi f d_{Rx,Tx}/c}, \tag{4}$$

with $\eta_{Rx,Tx}$ the channel direct current (DC) gain, defined as

$$\eta_{Rx,Tx} = \nu_{Rx,Tx} \frac{m+1}{2\pi} \cos^m \theta_{Rx,Tx}\, \frac{A_{Rx} \cos \psi_{Rx,Tx}}{d_{Rx,Tx}^2}, \tag{5}$$

where $\theta_{Rx,Tx}$, $\psi_{Rx,Tx}$ and $d_{Rx,Tx}$ are respectively the angle of emission, the angle of reception and the absolute distance between the RX and RX, as illustrated in Figure 2. A_{Rx} is the sensitive area of the photoreceiver, $\nu_{Rx,Tx}$ is the visibility factor, equal to one if the TX and RX are visible to each other and equal to zero otherwise (i.e. if there is a link blockage), whereas m is the Lambertian order of emission, which defines the directivity of the emitting light source and is equal to $-\ln 2 / \ln(\cos \Theta_{1/2})$, with $\Theta_{1/2}$ the semi-angle at half-power of the light source, called here half power beam width (HPBW).

The SNR of the received signal is then defined by

$$\mathrm{SNR} = \frac{\left(R_{PD}\eta_{Rx,Tx}P_t\right)^2}{\sigma_n^2}, \tag{6}$$

where R_{PD} is the photosensitivity of the photoreceiver, P_t is the optical power emitted by the light source of the OWC TX and σ_n^2 is the variance of electronic noise at the OWC RX. From (5) and (6), we can deduce that the SNR can be improved by playing on several degrees of freedom, both on the TX and RX sides of the OWC transceiver.

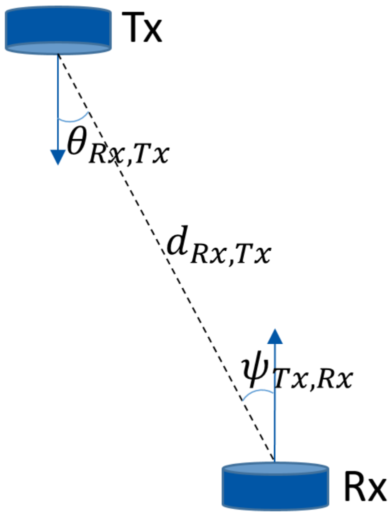

Figure 2 – Illustration of the OWC link geometry in a LOS scenario.

On the TX side:

- The emitted optical power (i.e. P_t) can be increased. However, this lever can only be used within the limits prescribed by the eye safety standards [IEC06, IEC14]. Note that in the 6G BRAINS project, we focus on NIR transmission. The visible illumination levels recommended by the standards in industrial environments are generally very high. However, such light sources of illumination act as noise sources from a light communication perspective, and they are easier to filter out when working in the NIR domain rather than in the visible light domain.
- It is possible to increase the directivity of the optical source (i.e. m). This degree of freedom allows to considerably improve the received optical power and thus the SNR in the axis of emission of the source. However, if m is too large, the emitted optical power decreases rapidly with the emission angle, thus limiting the coverage performance of the OWC channel sounder.

On the RX side:

- The photoreceiver used may be chosen so that its photosensitivity R_{PD} is as large as possible, especially in the NIR domain.
- It may also be chosen so that its sensitive area A_{Rx} is as large as possible. In practice, we can use the product $R_{PD}A_{Rx}$ as a reference metric to evaluate the contribution of these parameters to the received signal power.

These lists provide design rules for our OWC transceiver. In addition, as the objective is to evaluate the FR of the optical propagation channel, at least over a bandwidth relevant for data transmission purposes, our transceiver must have a bandwidth sufficiently large and flat. In practice, we propose within the framework of the 6G BRAINS project, to spread the development of the OWC transceiver in two steps. In a first step, we aim to reach a 3 dB modulation bandwidth of around 30 MHz. In a second step, we will try to reach a 3 dB modulation bandwidth of 200 MHz. In the present documents, the design and characterization of the first version of the OWC transceiver is detailed.

2.1.3 Benchmark of Existing OWC RXs

Before developing our own OWC transceiver, we listed and compared the performance of devices available on the market through a benchmark. The large variety of light emitting diodes (LEDs) and laser diodes available on the market allows for a multitude of combinations between emitted optical power, directivity and modulation bandwidth. We have therefore concluded that the most critical part of the OWC transceiver is its RX.

Table 1 lists the characteristics of the main photodetectors optimized for the NIR range available on the market, in terms of sensitivity, sensitive surface and bandwidth. We note that whatever the technology used – silicon positive-intrinsic-negative (Si PIN) or silicon avalanche photodiode (Si APD) –, the larger the sensitive area and the lower the bandwidth. We note moreover that the APD make it possible to reach higher sensitivities, with the detriment nevertheless of the available sensitive surface. Eventually, according to our comparison metric, the Hamamatsu© S12702-04 photoreceiver offers the best performance in the NIR range. Nevertheless, these performances can be improved with a custom design, as we are now going to detail.

Table 1 – Off-the-shelf photoreceiver benchmark

Reference	**Technology**	**Maximum sensitivity (R_{PD})**	**Sensitive area (A_{Rx})**	**Comparison metric ($R_{PD}A_{Rx}$)**	**Bandwidth**
Thorlabs© PDA100A	Si PIN	0.62 A/W @ 960 nm	100 mm²	62 A/W.mm²	DC – 11 MHz
Thorlabs© PDA8A2	Si PIN	0.56 A/W @ 820 nm	0.5 mm²	0.28 A/W.mm²	DC – 50 MHz
Hamamatsu© S12702-04	Si APD	15 A/W @ 800 nm	7.07 mm²	106 A/W.mm²	4 kHz – 80 MHz

2.2 Design and Characteristics of the Proposed OWC Transceiver

2.2.1 Transceiver architecture

Figure 3 presents the architecture of the OWC transceiver developed. It is composed of three main units: the optical TX, the optical RX and the power supply.

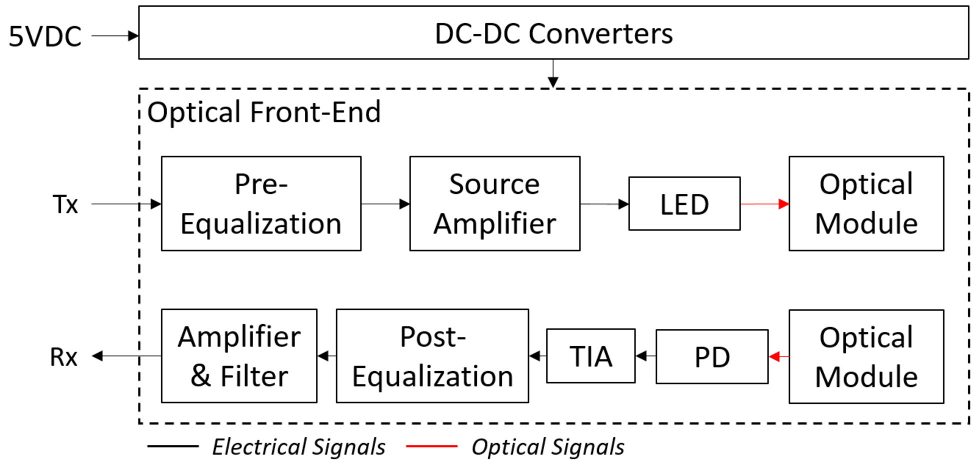

Figure 3 – Architecture of the developed OWC transceiver.

On the TX side, the drive signal produced by the channel sounder (see Section 4) is sent to the transceiver through the 'Tx' interface. This signal is first pre-equalized to cope with the light sources distortions and then amplified so that its current matches the light source characteristics. The light source then turns this current signal into an optical signal. An optical module, e.g. a lens, may finally be added to change the directivity of the light source depending on the measurements needs.

After free space propagation, the optical signal sent by the TX of one OWC transceiver is collected by the RX of another OWC transceiver. It may first be focused optical module to improve the collection performance, and is then turned into a current signal by the PD. This current signal is converted into a voltage signal and amplified by a transimpedance amplifier (TIA), then post-equalized to cope with the RX characteristic, and finally amplified again and filtered before being sent to the channel sounder through the ‘Rx’ interface.

Finally, the power supply unit consists in a set of DC-DC converters that turn a unique supply voltage of 5V into several voltages used at different stage of the transceiver, especially to bias the PD.

2.2.1 Main characteristics of the OWC Transceiver

Figure 4 shows the OWC transceivers built according to the architecture presented in Figure 3, whereas Table 2 highlights the main characteristics of the TX, RX and power supply units of the transceiver.

Each transceiver is equipped with a single power supply interface – an USB-C female port – which requires a 5V/1.2A source to power the board.

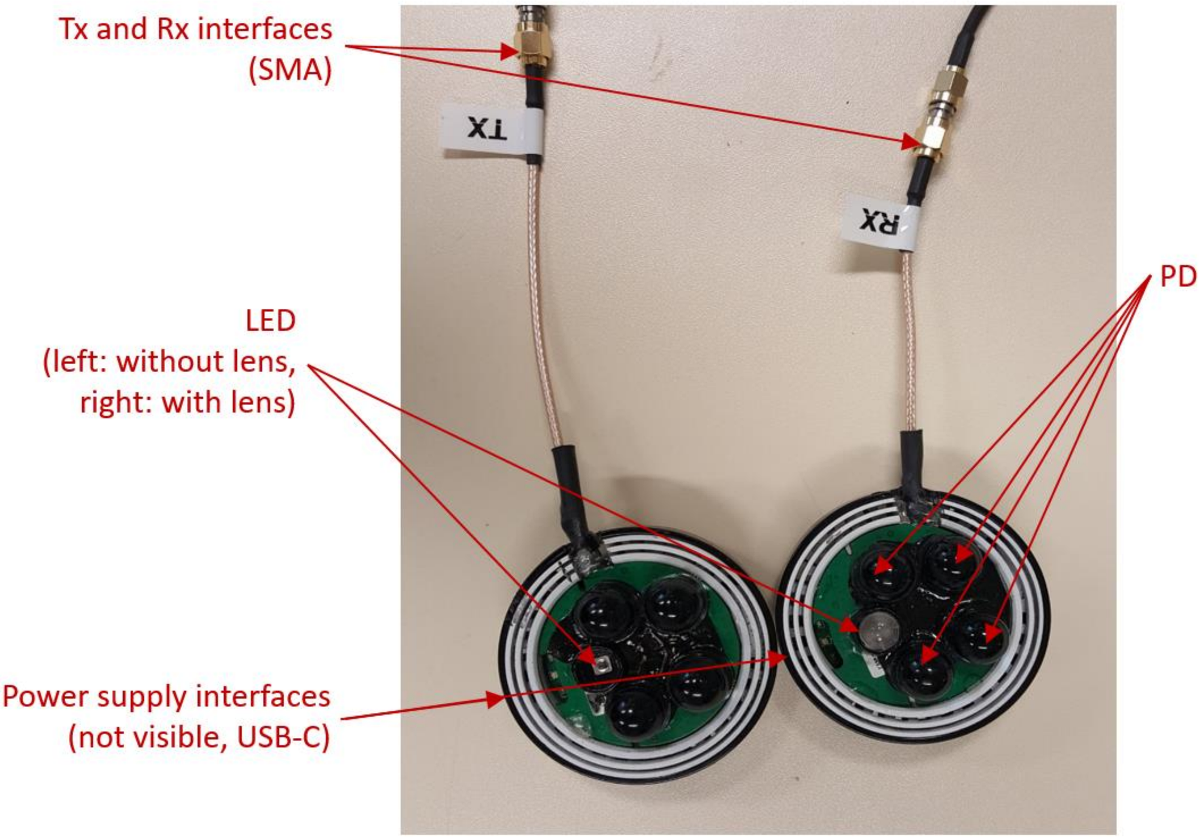

Figure 4 – View of two OWC transceivers, one used as TX, the other as RX.

Table 2 – Main characteristics of the OWC transceiver.

Power Supply Parameters	
Parameter	**Value**
Supply voltage	5 V
Supply current	1.2 A
Power supply interface	USB-C female
TX Parameters	
Parameter	**Value**
Driving current signal range	800 mA ± 400 mA
Transmitted optical power range	1080 mW ± 540 mW
Full angle at half power (without/with optical module)	90°/20°
Wavelength of operation	940 nm (910 nm to 950 nm)
Spectral width	40 nm
TX chain interface	SMA
RX Parameters	
Parameter	**Value**
Effective sensitive area	600 mm²
Photosensitivity width	400 nm (700 nm to 1100 nm)
Photosensitivity at 940 nm	0.62 A/W
Full angle at half sensitivity	60°
RX chain interface	SMA

On the TX side, a single LED is used and driven at an average current of 800 mA, corresponding to an average output optical power of around 1W. The LED driver supports a swing of ± 400 mA, so that the output optical power can vary linearly between 540 mW and 1620 mW, diffused over a full angle at half power of 90° when no focusing Fresnel lens is used, or 20° with a lens (i.e. HPBW $\Theta_{1/2}$ = 45° and 10° respectively). The wavelength of maximum power is 940 nm and the spectral width is around 40 nm, so that the adopted LED operates totally in the NIR domain.

On the RX side, four Hamamatsu© S6968 [HAM22] PD have been put in parallel to increase the sensitive area of the RX A_{Rx}. The signals produced by these PD are then summed up to get a single signal to process and send to the VNA. These PDs already have an integrated optical lens which limits the full angle at half-sensitivity to 60° but allows to collect more optical power so that they have an effective sensitive area of 150 mm² whereas their actual sensitive area is 26.4 mm². Eventually, our OWC transceiver thus have a total sensitive area of 600 mm², with a photosensitivity at 940 nm of 0.62 A/W, so that their collection power, evaluated by the product $R_{PD}A_{Rx}$, is clearly larger than that of off-the-shelf photoreceivers, as illustrated by Figure 5.

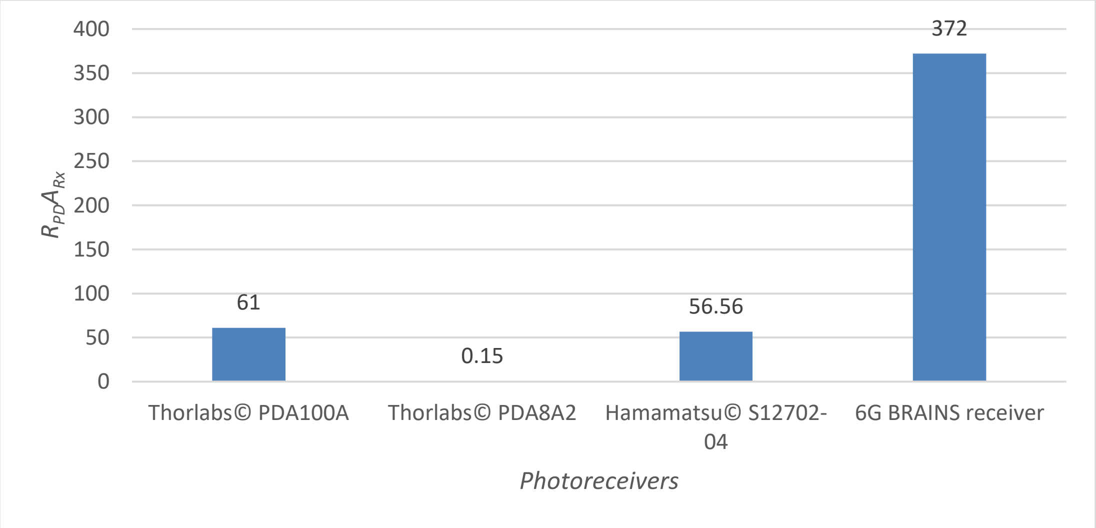

Figure 5 – Comparison of the proposed OWC RX with off-the-shelf photoreceivers.

2.3 OWC Transceiver Characterization

As detailed in Section 2.1, it is necessary to characterize our OWC transceiver before using it to measure the FR of the optical propagation channel. In particular, we need to evaluate its FR $H_{sys}(f)$, or at least the link FR $H_{ref}(f)$ in a reference scenario.

Figure 6 illustrates the set-up used to evaluate $H_{ref}(f)$. One transceiver, used as TX is connected to the output of an Agilent E5071C VNA, whereas another transceiver used as RX is connected to the input of the VNA. The VNA is programmed to output a driving sinewave of power 0 dBm [MHH19], of frequency ranging linearly from f_{min} = 100 kHz to f_{max} = 50 MHz, and to compute at the same time the S_{12} parameter which frequency evolution is displayed on the screen and can be recorded. Note that in Figure 5, the FR displayed is that of an NLOS link relying on the reflection of the transmitted optical signal on the palm of the hand that is on top of both transceivers. To estimate $H_{ref}(f)$, the setup adopted was slightly different, as both transceivers were facing each other ($\theta_{Rx,Tx} = \psi_{Rx,Tx} = 0$) and placed at a reference distance d_{ref} = $d_{Rx,Tx}$ = 40 cm, chosen so that the observed FR does not exhibit linear distortions.

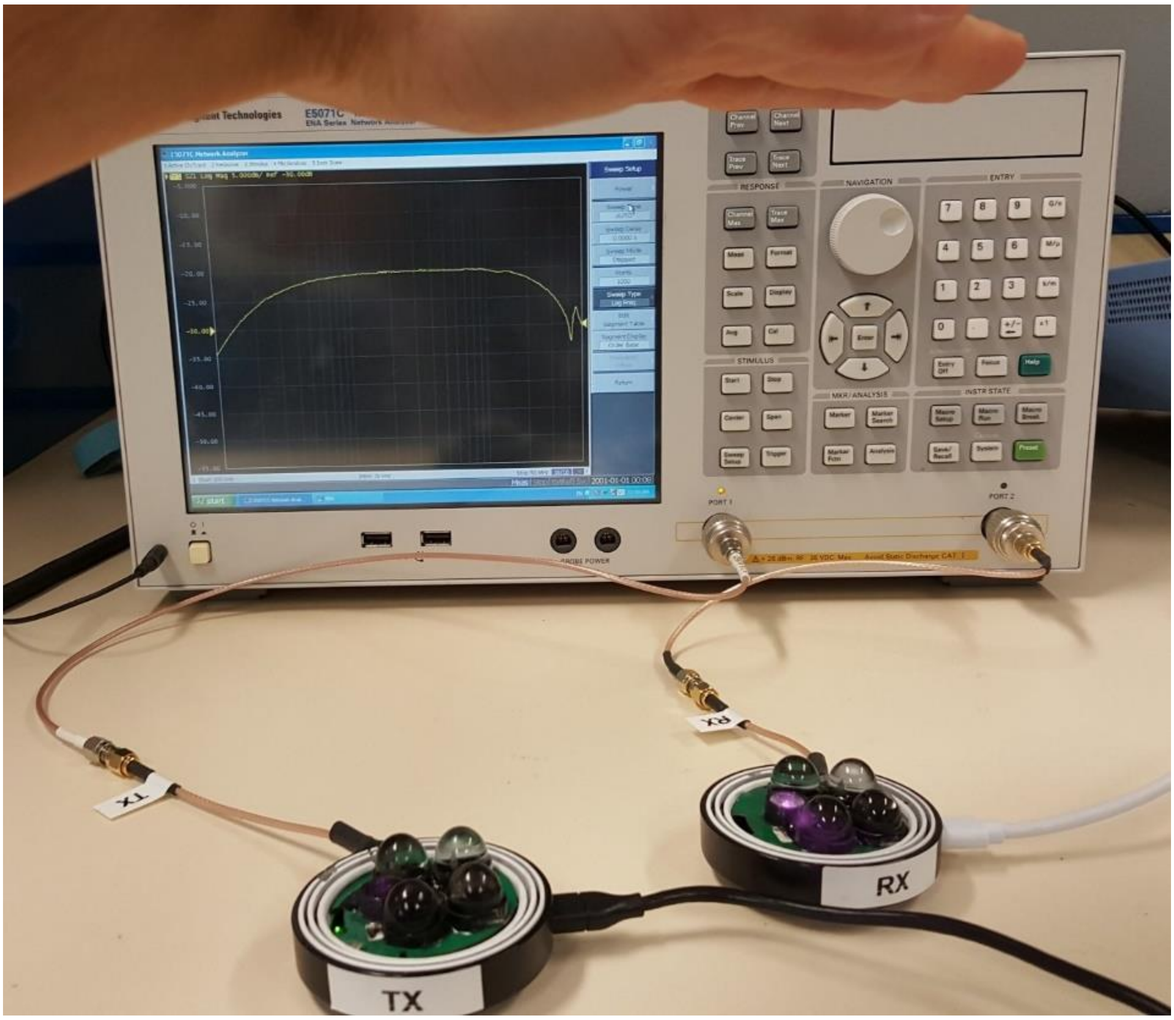

Figure 6 – Setup used to characterize the FR of the OWC transceiver.

In practice, the FR observed in this reference scenario is plotted in Figure 7. We can see that it is relatively flat over most of the frequency range, with a low pass behavior from around 30 MHz, which comes from the limited modulation bandwidth of the NIR LED used in the TX, and a high pass behavior below around 300 kHz, which has been deliberately added to cut ambient light sources.

If we define the X dB system bandwidth as the frequency range over which the magnitude is higher than its maximum value minus X dB, then we can conclude from the calibration tests that our OWC transceiver has a 3 dB bandwidth of 36 MHz and a 6 dB bandwidth of 47.5 MHz. The resulting FR can then be used directly to correct future link measurements, or indirectly after modeling its behavior using for example a curve fitting function or a state-space representation.

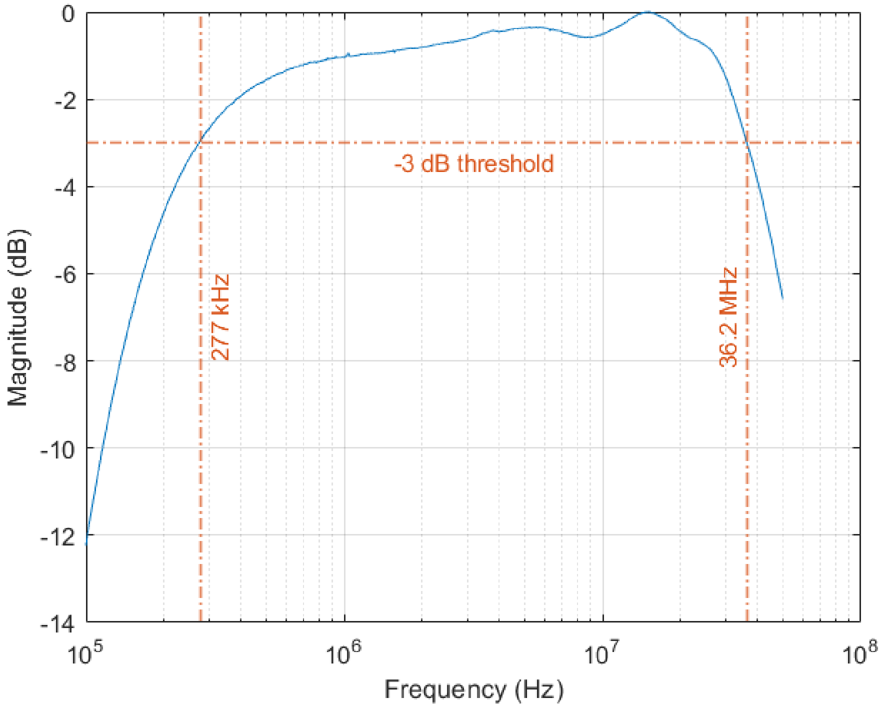

Figure 7 – FR $H_{ref}(f)$ of the OWC link in the reference scenario (blue curve). The 3 dB bandwidth of the system is illustrated with the orange dashed-dotted lines.

3 Multiband RF UWB Dual-Polarized Sub-6 GHz, mmWave, and Sub-THz Channel Sounder

Channel sounding consists of transmitting a known signal and analyzing the received echoes from the environment to study the propagation characteristics in a certain environment. According to the excitation signal, channel sounder architectures can be classified, between others, into two categories: *narrowband* and *wideband*. The first one uses a narrowband test signal, e.g., a single tone to measure the FR of the channel in a single frequency. Broadband measurements can be conducted by sweeping the spectrum with a single tone. However, this is time consuming and requires a static scenario during the measurements. Examples of such an architecture are VNA based channel sounders.

On the other hand, wideband channel sounders operate with broadband signals measuring instantaneously the complete bandwidth. The excitation signals can be designed in the time domain or frequency domain. Examples are the pseudo-random binary sequence (PRBS) and multicarrier signals, such as orthogonal frequency division multiplexing (OFDM) signals. One of the principal advantages of the PRBS is the very low peak-to-average power ratio (PAPR) that permits a better utilization of the available power on the power amplifiers (very limited in mmWave and sub-THz systems) and is less prone to generate non-linear distortions. On the other hand, multicarrier signals offer more degrees of freedom on their design but suffer from a high PAPR which causes saturation in power amplifiers, forcing to reduce the power efficiency. Different techniques can be applied to reduce the PAPR, e.g., clipping and phase optimization.

The RF part of the TU-Ilmenau dual-polarized channel sounder used within 6G BRAINS is based on a PRBS chipset [MHD14], and the OWC part in a programmable multicarrier signal with optimized phases to reduce non-linearities.

3.1 Multiband Multidimensional Channel Sounding

The goal of multidimensional channel sounding is to provide the necessary data to jointly estimate the different geometrical properties of the multi-path components of the channel. Multiband multidimensional channel sounding intends to achieve the same goal but over several bands with different propagation characteristics and system aspects, minimizing the influence of the measurement system on the results.

The purposes of the measurements within the WP3 of 6G BRAINS are the characterization of propagation by comparison at different bands and the validation of the RT model obtained in [6GB31]. While the system aspects as bandwidth and directivity differ considerably within the targeted bands, the investigated geometrical parameters of the multipath components are still the same. Therefore, measurements must be taken with at least the resolution of the targeted system with higher resolution, in this case, the sub-THz. It is still challenging to measure instantaneous bandwidths similar to the full available block of spectrum at this band due to limitations in the current state of the art on channel sounding. However, following the IEEE 801.15.3d [PKH20] standard, we can find that at sub-THz, there are 32 channels with 2.16 GHz bandwidth (that can be combined) into a single massive 69.12 GHz bandwidth, and therefore, significant measurements can still be done with 4 GHz bandwidth.

For an ease of nomenclature, from now on we define sub-6 GHz as the band centered at 6.75 GHz, mmWave or 70 GHz to the one centered at 74.25 GHz, and sub-THz or 190 GHz to the one centered at 187.5 GHz.

To compare the results in the different bands, the channel sounder must have similar characteristics in the different measurement domains over:

- bandwidth for delay resolution,
- antenna gain (directivity) for DoD and DoA resolution, and
- sampling rate for Doppler analysis if possible.

3.2 The TU-Ilmenau Dual-Polarized Ultra-Wideband Channel Sounder Architecture

The macro-architecture consists of three units: a **TX unit**, a **RX unit**, and a **server unit** dedicated to control the measurements. In addition, we distinguish three different types of signals and planes distributed on the different units:

- measurement related (in blue),
- synchronization related (green), and
- control related (orange).

Further details on each unit and planes are discussed in the following subsections.

The **TX** and **RX units** are mounted over positioners that can scan the angular domain in azimuth and elevation. All the cables and connectors are fixed to avoid phase noise due to movement. In addition, the distribution of the synchronization signals is achieved over fiber optical cables also to minimize phase noise due to the displacement of the cables during rotation of the positioners.

3.2.1 Measurement Plane

The measurement plane consists of commercial UWB units (Ilmsens, shown in Figure 9(a)) and in-house designed and assembled up and down converter units to the desired frequencies. Each unit consists of a single TX channel and two RX channels. This was originally designed for mono-static radar applications. However, in this set-up, the two RX channels are used for polarization. Unlike the original application, we have implemented a bi-static set-up with two different units distributed at TX and RX side. Therefore, for polarization it is implemented a switch at the TX side to alternate between the orthogonal components, and two parallel channels are measuring simultaneously both polarizations at the RX.

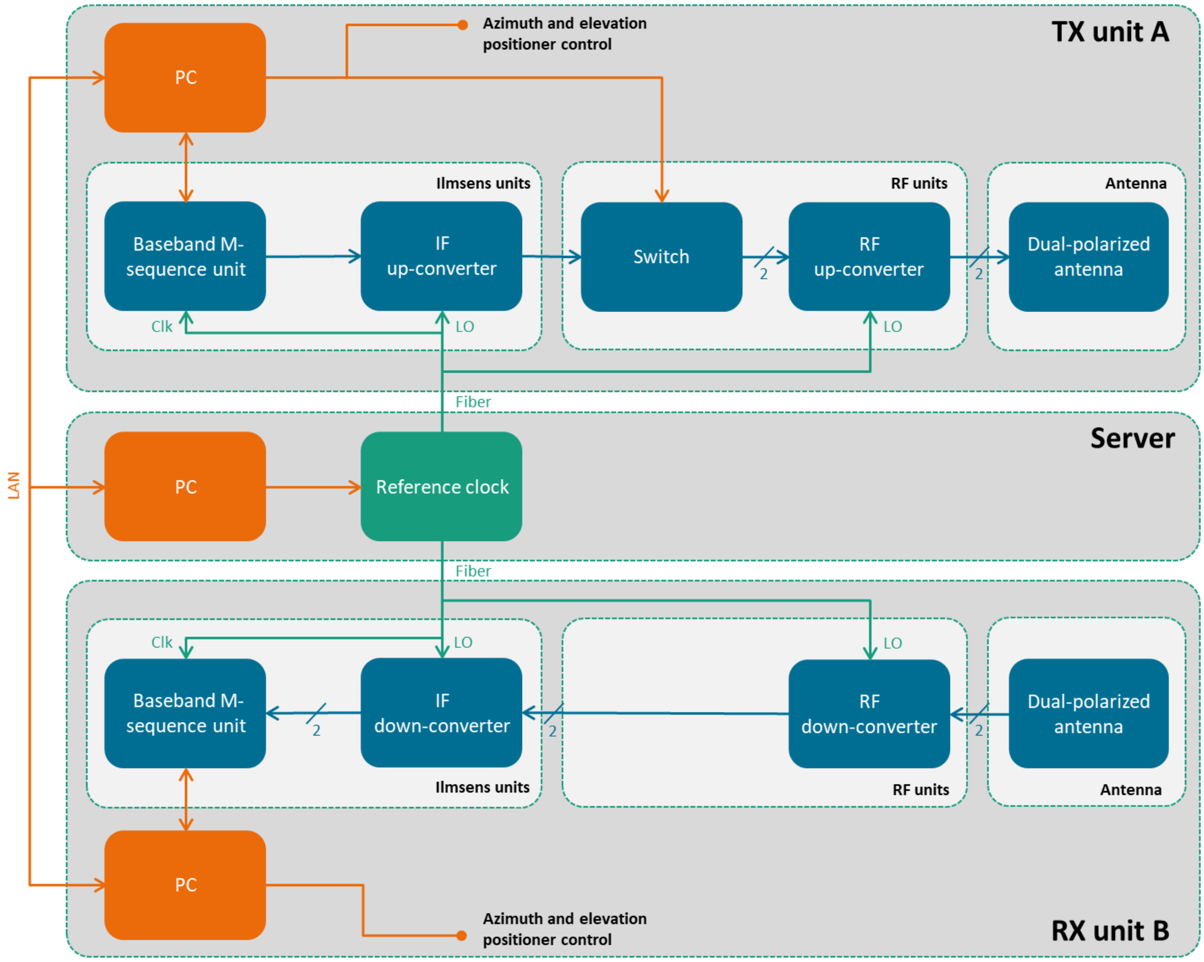

Figure 8 – Physical macro units (in dark gray) of a single band channel sounder, physical units inside of the macro units (in light gray) and the different planes: measurements (blue), synchronization (green), and control (orange).

(a) (b) (c)

Figure 9 – (a) Top view of the base-band modules. (b) Detail on the interconnection of the baseband and intermediate frequency (IF) stages in the front-side. (c) View of the backside with the clock and interfaces.

3.2.1.1 Baseband

The excitation signal is a 12-bit maximum-length binary sequence (MLBS), also known as M-sequence with $M_l = 12$ bits, a sub-class of PRBS. The particularity of these type of binary sequences is that they are periodic and reproduce any sequence that can be generated with a shift register. The number of zeros and ones in the binary sequence are practically equal, which generates a flat spectrum and provides a good crest factor in comparison to other broadband spread spectrum signals as multi-sinus (OFDM-like).

The length of the sequence is $2^{M_l} - 1 = 4095$ bits. The input clock to the units defines the bandwidth (rate) and the IF frequency. The bandwidth and the length of the sequence also define the unambiguity measurement range, i.e., the range in which all the echoes arrive within one period of the excitation signal.

The units operate with a pre-scaler and a sub-sampler that reduces the amount of channel impulse responses (CIRs) per second that can be measured, also reducing the Doppler resolution.

3.2.1.2 IF Stage

The baseband modules have an integrated up and down conversion stage to IF. The IF frequency is determined by the same clock frequency used for the baseband units that determine the measurement bandwidth. Since the up and down converters operate with an input frequency of 6.75 GHz, the baseband outputs are connected to the IF as shown in Figure 9.

3.2.1.3 RF Stage

The up and down converters at the different frequencies were in-house designed and mounted. Due to the dual polarized architecture, at the RX side they consist of two parallel chains after an orthomode transducer (OMT). On the other hand, at the TX, there are two different designs depending on the band, however, in both cases the alternation between TX polarizations is carried out with a switch, which can be either at IF (sub-THz at 190 GHz showed in Figure 10a) or RF (mmWave up-converter at 70 GHz showed in Figure 10(b)).

The up and down converters use the same local oscillator (LO) as the Ilmesens units to keep coherency. This LO defines the baseband bandwidth, the IF frequency, and scaled with internal multipliers, the RF frequency.

Internal attenuators and driver amplifiers, as well as some filters are neglected in the schematics for simplification.

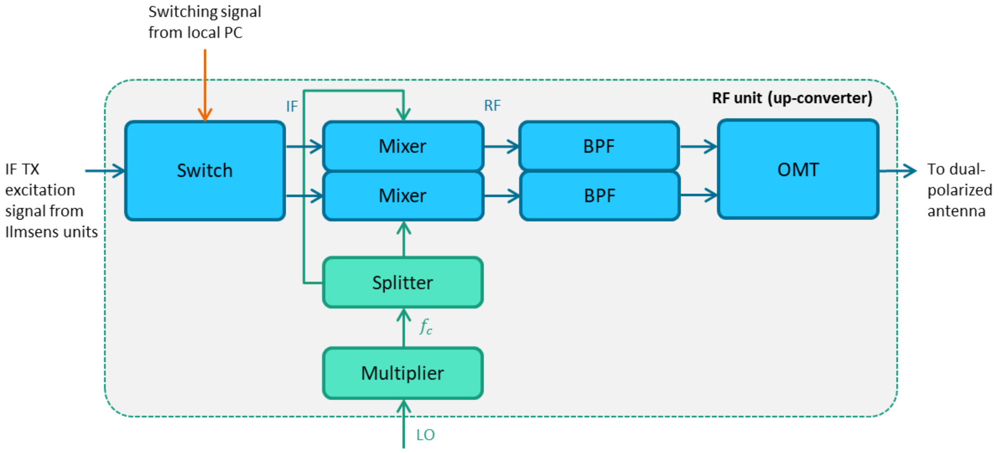

(a)

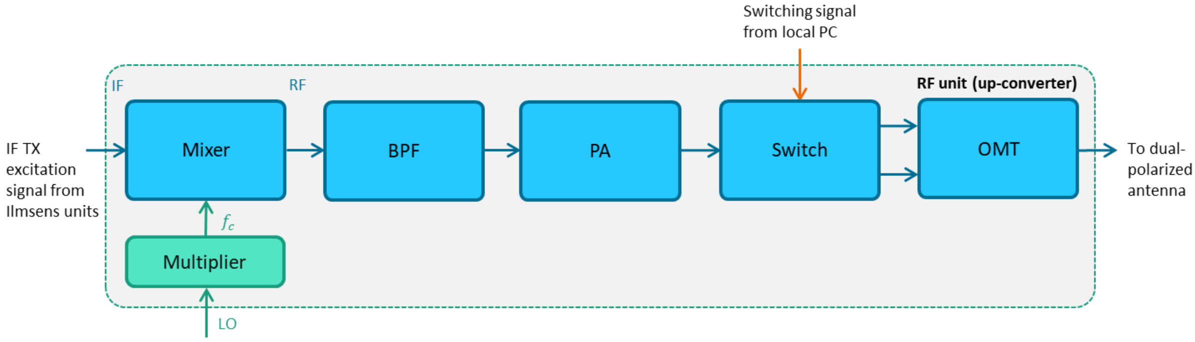

(b)

Figure 10 – Schematic of the upconverter (a) in the sub-THz band and (b) in the mmWave band.

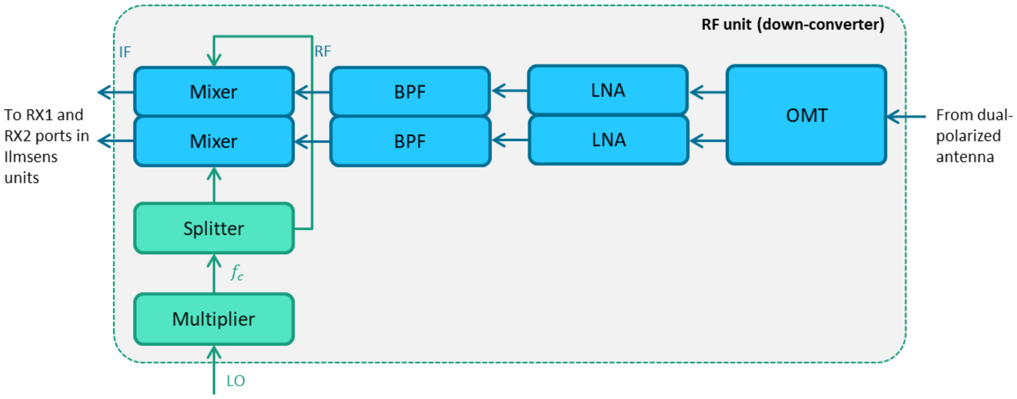

Figure 11 – Schematic of the down-converters in the mmWave and sub-THz bands.

The up and downconverters at mmWave and sub-THz are fed with an input reference of 6.75 GHz and 7.5 GHz, respectively.

3.2.1.4 Antennas

The resolution in the angular domain is determined by the directivity of the antennas. This also determines de minimum scanning step in the angular domain, and therefore, the required measurement time.

Ideally, the antennas must have the same radiation pattern in the different bands. However, this is difficult to obtain, not only because of the variation in the patterns between different frequencies, but also because of the variation of the FR of the antennas themselves. Given this practical limitation, we have selected dual-polarized 15° HPBW horn antennas with the most similar patterns possible at mmWave and sub-THz. Such a high directivity is also required at sub-THz to compensate the isotropical path-loss and extend the measurement range. On the other hand, at sub-6 GHz, 30° HPBW antennas were implemented due to the physical size. The measured antenna patterns in the different frequencies are shown in Figure 12.

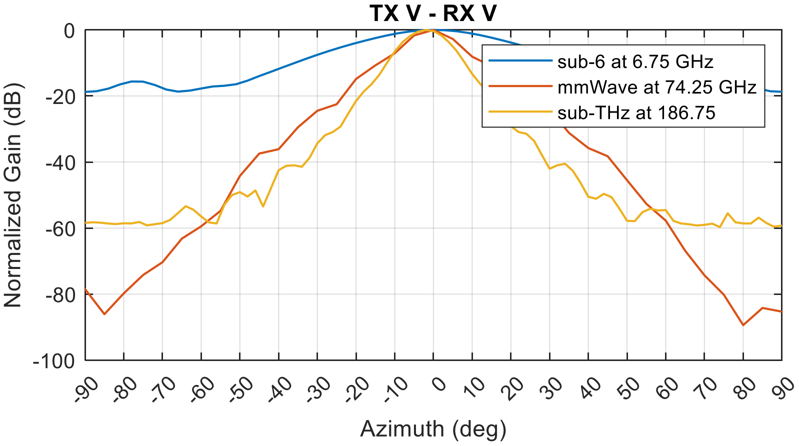

Figure 12 – Measured antenna pattern of the different RF bands in the vertical polarization.

The measured synthetic pattern of the antenna after rotation with 15° steps is shown in Figure 13(a). Two different effects need to be analyzed: the oscillation within the band, and the difference between bands. The first case shows that there is a difference on RX power depending on the impinging angle (same occurs at the TX side with the angle of departure). This is because even if the specifications of the antennas describe a 15° HPBW, in practice it seems to be narrower. This will affect the calculation of the power delay profile (PDP) from a synthetic wider pattern and parameters as DS calculated from them will also be inaccurate. While this difference is neglected at sub-6 GHz since the scanning steps are half of the HPBW of the antenna, this difference can be of approx. 3 dB in the sub-THz band. Figure 13(b) shows the pattern with 10° steps, where the variations on gain accordingly to the angle is minimum. However, scanning with such a step increases measurement times to unpractical numbers for double side resolution in complex scenarios.

The second analysis is the comparison between bands, where a difference on RX power between the mmWave and sub-THz can be observed for the same DoA or DoD. This difference is also minimized with 10° scanning steps.

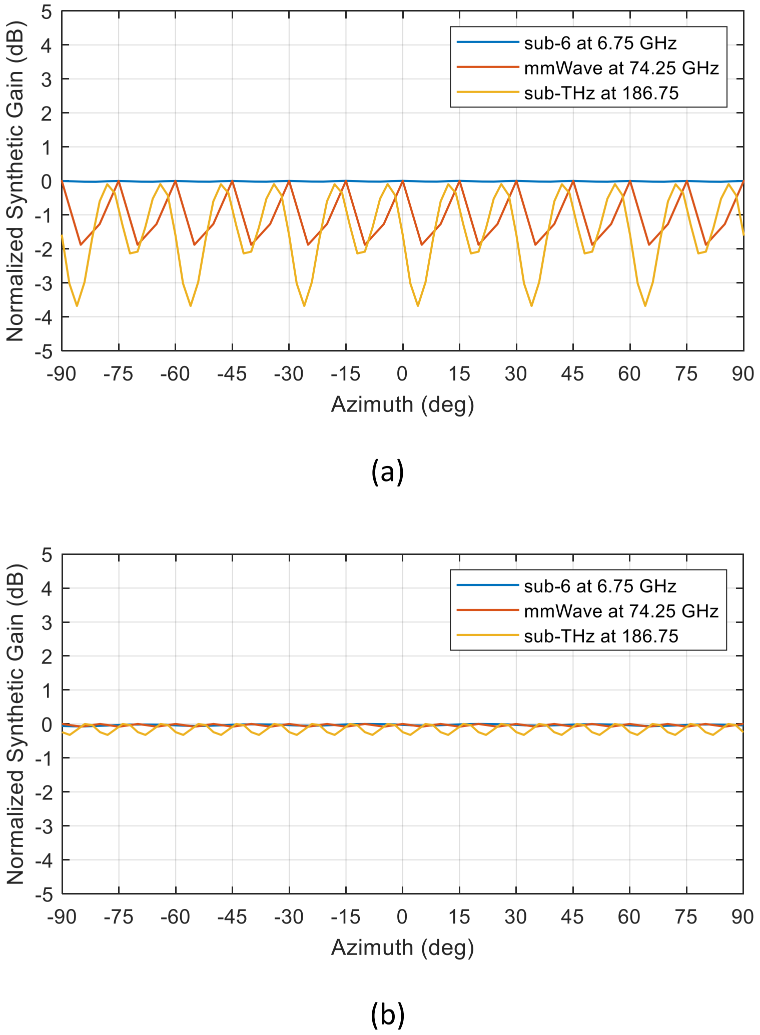

Figure 13 – Synthetic pattern at the different RF measured bands with (a) 15° rotation steps, and (b) 10° rotation steps.

3.2.2 LO Generation and Distribution Plane

The 200 MHz reference clock is generated in the server unit with the programable frequency synthesizer APSYN420 and converted to fiber for the distribution to the TX and RX units.

In the unit A and B, it is converted back to RF and distributed to the wideband RF synthesizers LMX2595, that accordingly to the band, generate a 6.75 GHz or 7.5 GHz reference clock, as shown in Figure 14.

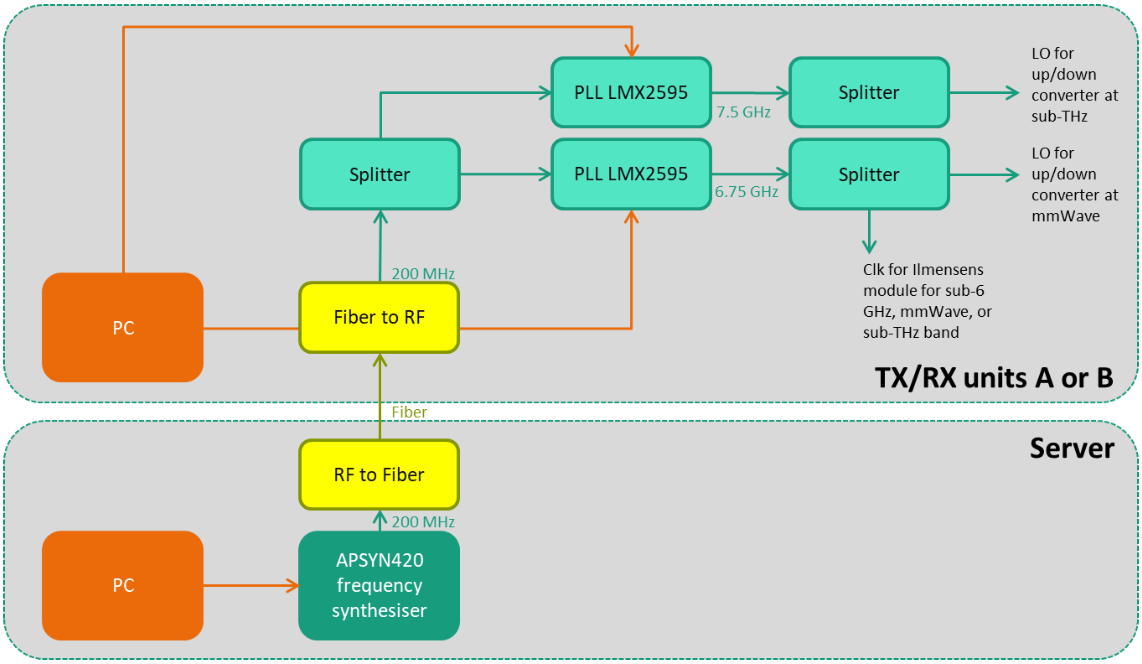

Figure 14 – Generation and distribution of the reference clock.

3.2.3 Control Plane

The control plane consists of a master computer located in the server unit, and local computers at the TX and RX. The computer in the server is in charge of synchronizing the TX and RX computers and to configure the reference clock in the server.

The local computers are connected to the Ilmsens units to perform and locally store the measurements. In addition, they configure the LMX2595 and control the polarimetric switching signals and the positioners.

3.2.4 Smart Utilization of Resources

The amount of Ilmsens modules needed to measure in a bi-static configuration N_f different bands can be reduced by configuring each module to transmit at a certain band and receive in a different one [MHD16]. Therefore, in the macro-architecture there are not anymore TX or RX units, but unit A and B.

Hence, in principle, N_f different Ilmsens modules are necessary to measure N_f different bands with certain engineering, as shown in Figure 28: a single Ilmsens module in unit A to receive the sub-6 GHz, and to transmit simultaneously at mmWave and sub-THz. On the other side, in unit B, there are two Ilmsens modules. One is in charge of receiving mmWave and transmitting one of the polarizations of sub-6 GHz, and the other one is in charge of receiving the sub-THz and transmitting the remaining polarization at sub-6 GHz.

3.3 Channel Sounder Specifications

The specifications of the quad-band channel sounder covering the sub-6 GHz, mmWave, sub-THz, and OWC bands are summarized in Table 3.

Table 3 – Technical characteristics of the quad-band channel sounder.

Band	**Excitation signal**	**Centre frequency / wavelength**	**Frequency range**	**BW (null-to-null)**	**BW after calibration**	**Measured DR at 5 m distance**	**HPBW**
Sub-6 GHz	M-sequence	6.75 GHz	3.375 GHz – 10.125 GHz	6.75 GHz	4 GHz		30°
mmWave	M-sequence	74.25 GHz	70.875 GHz – 77.625 GHz				15°
Sub-THz	M-sequence	186.75 GHz	183.375 GHz – 190.125 GHz				15°
OWC	Multisinus	940 nm	-	250 MHz	50 MHz	41.51 dB	70°

3.4 Processing of the Measurements

3.4.1 Identification of the CIR From Measurements

The RX signal in the port p (related to the polarization) after multipath propagation, with $l = \{1, \dots L-1\}$ different paths, can be modelled as

$$\begin{aligned} y^p(t) &= \sum_{l=0}^{L-1} g_{RX}^p(\phi-\phi_l,\theta-\theta_l)g_{TX}^p(\varphi-\varphi_l,\vartheta-\vartheta_l)\,\alpha_l\gamma_l^p s(t-\tau_l)+\eta(t), \\ &= \underbrace{\sum_{l=0}^{L-1} g_{RX}^p(\phi-\phi_l,\theta-\theta_l)g_{TX}^p(\varphi-\varphi_l,\vartheta-\vartheta_l)\,\alpha_l\gamma_l^p \delta(t-\tau_l)}_{h^p(t)} * s(t)+\eta(t), \end{aligned} \tag{7}$$

Where $s(t)$ is the excitation signal, α_l is the attenuation of the signal due to free-space path-loss, γ_l^p is the scattering loss, $g_{TX}^p(\varphi,\vartheta)$ and $g_{RX}^p(\phi,\theta)$ are the TX and RX antenna patterns, respectively, in the port p for the azimuth ϕ and elevation θ, and (ϕ_l,θ_l) and (φ_l,ϑ_l) are the azimuth and elevation of arrival and departure, respectively. Finally, $\eta(t) \sim N(\mu = 0, \sigma_\eta)$ is additive white Gaussian noise.

The RX signal $y^p(t)$ can be described as the convolution between the multi-path channel $h^p(t)$ and the excitation signal $s(t)$.

To identify the CIR, the sampled signal at the RX is then cross correlated with a copy of the TX signal. The cross-correlation process is conducted in the frequency domain by multiplying the measured spectrum $Y(f) = H(f)S(f) + \eta(f)$ with the complex conjugate of the TX signal spectrum. Due to the correlation properties of the TX signal, a pseudo noise (PN) sequence, $S(f)S^*(f) = 1 \;\forall\, f$ within the measurement bandwidth:

$$\begin{aligned}\widehat{H}(f) &= Y(f)S^*(f), \\ &= H(f)\ \underbrace{S(f)S^*(f)}_{1\ \forall f \in \left\{-\frac{B}{2},\dots,\frac{B}{2}\right\}} + \underbrace{\eta(f)S^*(f)}_{\tilde{\eta}(f)}.\end{aligned} \tag{8}$$

The measured channel $\tilde{h}(\tau)$ sampled in the time domain $\Delta\tau = \frac{1}{B}$ with a bandwidth B can be represented as

$$\begin{aligned}&\hat{h}^p(\tau) = \sum_{k=0}^{K-1} \dots \\ &\underbrace{\left[\sum_{l=0}^{L-1} g_{RX}^p(\phi - \phi_l, \theta - \theta_l) g_{TX}^p(\varphi - \varphi_l, \vartheta - \vartheta_l)\, \alpha_l \gamma_l^p \frac{1}{\Delta\tau} \operatorname{sinc}\left(\frac{k\Delta\tau - \tau_l}{\Delta\tau}\right) + \hat{\eta}(k\Delta\tau)\right]}_{a_k} \dots \\ &\delta(\tau - k\Delta\tau),\end{aligned} \tag{9}$$

where $K = 2^{M_l} - 1$ is the total amount of samples in the delay domain with $M_l = 12$ bits being the length of the M-sequence in this configuration of the channel sounder. Each sample a_k is the summation of the different delayed multipath components within the delay sample $\Delta\tau$ and the measurement noise. It is important to notice the effect of the sidelobes of the $\operatorname{sinc}(\cdot)$ function resulting from the bandlimited cross correlation during (8). It is clear from (9) that by increasing the measurement bandwidth B, $\Delta\tau \to 0$ and each measured sample a_k will be less affected by the sidelobes of the delayed multipath components and contain only the information of the l^{th} multipath component arriving in that specific delay.

In a similar manner, the angular domain is sampled by rotating directive antennas in the azimuth and elevation at TX and RX. The rotation steps $\Delta\phi$, $\Delta\theta$, $\Delta\varphi$, and $\Delta\vartheta$ correspond to the azimuth and elevation at RX, and azimuth and elevation at TX, respectively. Hence, the measured CIR in a single snapshot can be modelled as

$$\begin{aligned}&\hat{h}^p(\tau, \phi, \theta, \varphi, \vartheta) = \sum_{i=0}^{I-1} \sum_{j=0}^{J-1} \sum_{m=0}^{M-1} \sum_{n=0}^{N-1} \sum_{k=0}^{K-1} \dots \\ &\underbrace{\left[\begin{array}{c}\displaystyle\sum_{l=0}^{L-1} g_{RX}^p(\phi - i\Delta\phi - \phi_l, \theta - j\Delta\theta - \theta_l) g_{TX}^p(\varphi - m\Delta\varphi - \varphi_l, \vartheta - n\Delta\vartheta - \vartheta_l) \dots \\ \displaystyle\alpha_l \gamma_l^p \frac{1}{\Delta\tau} \operatorname{sinc}\left(\frac{k\Delta\tau - \tau_l}{\Delta\tau}\right) + \hat{\eta}(k\Delta\tau)\end{array}\right]}_{a_{i,j,k,m,n}} \dots \\ &\delta(\tau - k\Delta\tau)\delta(\phi - i\Delta\phi)\delta(\theta - j\Delta\theta)\delta(\varphi - m\Delta\varphi)\delta(\vartheta - n\Delta\vartheta),\end{aligned} \tag{10}$$

where $p = \{1, \dots P = 4\}$ represents the TX-RX polarimetric channel $\{\phi\phi, \phi\theta, \theta\phi, \theta\theta\}$, $i = \{1, \dots, I\}$ and $j = \{1, \dots, J\}$ are the index of the scanning direction in azimuth and elevation at the TX, and $m = \{1, \dots, M\}$ and $n = \{1, \dots, N\}$ at the RX.

For the sake of simplicity, (10) can be represented as

$$\begin{aligned}&\hat{h}^p(k\Delta\tau, i\Delta\phi, j\Delta\theta, m\Delta\varphi, n\Delta\vartheta)\\&=\sum_{l=0}^{L-1} g_{RX}^p(\phi - i\Delta\phi - \phi_l, \theta - j\Delta\theta - \theta_l) g_{TX}^p(\varphi - m\Delta\varphi - \varphi_l, \vartheta - n\Delta\vartheta - \vartheta_l) \dots\\&\qquad \alpha_l \gamma_l^p \frac{1}{\Delta\tau} \operatorname{sinc}\left(\frac{k\Delta\tau - \tau_l}{\Delta\tau}\right) + \hat{\eta}(k\Delta\tau).\end{aligned} \tag{11}$$

Finally, all the measurements are arranged and stored in a multidimensional array

$$\hat{\mathcal{H}} \in \mathbb{C}^{K\times P\times I\times J\times M\times N}. \tag{12}$$

3.4.2 Noise Floor Estimation and Removal

All the measurements are always contaminated with noise. The source can be internal or external. We focus in the first case, where noise is usually modelled as an additive random process with a Gaussian distribution, $\eta(t) \sim N(0, \sigma_\eta)$.

Therefore, during the analysis of the measured CIR, the channel samples need to be separated from pure noise samples in order not to take noise as possible multipath components. Otherwise, the comparison to RT simulated CIRs can be misleading and figures as delay spread can be severely affected.

In addition, if the channel sounder is equipped with an automatic gain controller (AGC) at the RX, the compensation of the AGC in a post-processing step increases the measured noise floor, since the measured CIR is multiplied by the inverse of the attenuation of the AGC. This is problematic if the PDPs of different scans in the angular domain are combined to obtain synthetically the PDP of a wider pattern.

Therefore, before any processing or analysis is done, the noise floor is independently estimated and removed for each measured CIR $\hat{h}^p(k\Delta\tau, i\Delta\phi, j\Delta\theta, m\Delta\varphi, n\Delta\vartheta)\ \forall\, k$ in the polarimetric port p with the antennas pointing in the (i, j, m, n) directions.

The estimation method utilizes the null-hypothesis test. Because of the random nature of the noise, once the noise level is estimated a certain margin is adopted to remove all the samples below the noise floor level plus this margin to not take noise samples as multipath components. The margin adopted is of 10 dB, which guarantees a probability of taking noise as a multipath of 0.00005 [DMT21].

It is important to remark that after the noise floor removal, the remaining CIR samples are still contaminated with noise.

3.4.3 Total Received Power

The total received power for a certain polarization p can be calculated as the summation of all the energy in the different dimensions

$$P=\sum_{p=1}^{P}\sum_{m=0}^{M-1}\sum_{n=0}^{N-1}\sum_{i=0}^{I-1}\sum_{j=0}^{J-1}\sum_{k=0}^{K-1}|\hat{h}^{p}(k\Delta\tau,i\Delta\phi,j\Delta\theta,m\Delta\varphi,n\Delta\vartheta)|^{2}. \tag{13}$$

3.4.4 Marginal Power Profiles From Directive Measurements

The 2-dimensional marginal power profiles can be calculated for certain dimensions by summing the power of the measured CIR in the remaining ones. For example, the power azimuth/delay profile (PADP) at the RX is calculated as

$$\mathrm{PADP}^{p}(k\Delta\tau,i\Delta\phi)=\sum_{m=0}^{M-1}\sum_{n=0}^{N-1}\sum_{j=0}^{J-1}|\hat{h}^{p}(k\Delta\tau,i\Delta\phi,j\Delta\theta,m\Delta\varphi,n\Delta\vartheta)|^{2}. \tag{14}$$

The single dimension marginal power profiles are calculated in a similar manner. Examples of the most relevant power profiles are the PDP, power azimuth profile (PAP), and power elevation profile (PEP):

$$\begin{aligned}
\mathrm{PDP}^{p}(k\Delta\tau)&=\sum_{m=0}^{M-1}\sum_{n=0}^{N-1}\sum_{i=0}^{I-1}\sum_{j=0}^{J-1}|\hat{h}^{p}(k\Delta\tau,i\Delta\phi,j\Delta\theta,m\Delta\varphi,n\Delta\vartheta)|^{2},\\
\mathrm{PAP}_{\mathrm{RX}}^{p}(i\mathit{\Delta}\phi)&=\sum_{m=0}^{M-1}\sum_{n=0}^{N-1}\sum_{j=0}^{J-1}\sum_{k=0}^{K-1}|\hat{h}^{p}(k\Delta\tau,i\Delta\phi,j\Delta\theta,m\Delta\varphi,n\Delta\vartheta)|^{2},\\
\mathrm{PEP}_{\mathrm{RX}}^{p}(j\mathit{\Delta}\theta)&=\sum_{m=0}^{M-1}\sum_{n=0}^{N-1}\sum_{i=0}^{I-1}\sum_{k=0}^{K-1}|\hat{h}^{p}(k\Delta\tau,i\Delta\phi,j\Delta\theta,m\Delta\varphi,n\Delta\vartheta)|^{2}, \qquad (15)\\
\mathrm{PAP}_{\mathrm{TX}}^{p}(m\mathit{\Delta}\varphi)&=\sum_{n=0}^{N-1}\sum_{i=0}^{I-1}\sum_{j=0}^{J-1}\sum_{k=0}^{K-1}|\hat{h}^{p}(k\Delta\tau,i\Delta\phi,j\Delta\theta,m\Delta\varphi,n\Delta\vartheta)|^{2},\\
\mathrm{PEP}_{\mathrm{TX}}^{p}(n\mathit{\Delta}\vartheta)&=\sum_{m=0}^{M-1}\sum_{i=0}^{I-1}\sum_{j=0}^{J-1}\sum_{k=0}^{K-1}|\hat{h}^{p}(k\Delta\tau,i\Delta\phi,j\Delta\theta,m\Delta\varphi,n\Delta\vartheta)|^{2}.
\end{aligned}$$

If no polarization is discriminated, the contributions in the different polarizations are summed up, for example for the $\mathrm{PDP}(k\Delta\tau)=\sum_{\forall p}\mathrm{PDP}^{p}(k\Delta\tau)$.

3.4.5 Calculation of Spreads

As the name indicates, the spread values as delay spread (DS), azimuth spread (AS), and elevation spread (ES) represent how the energy is dispersed in the channel in those dimensions, i.e., the spreading characteristics of the channel. These values are used for system design (e.g., DS for calculation of guard intervals and angular spreads for antenna characteristics) and for channel models (e.g., large-scale parameters in spatial channel models as the 3GPP).

The root mean square (RMS) spread values are calculated from the single dimension power profiles from (20). For example, the RMS DS is calculated as

$$\mathrm{DS} = \sqrt{\frac{\sum_{\forall k}(k\Delta\tau)^2 \cdot \mathrm{PDP}(k\Delta\tau)}{\sum_{\forall k}\mathrm{PDP}(k\Delta\tau)} - \left(\frac{\sum_{\forall k} k\Delta\tau \ \cdot \mathrm{PDP}(k\Delta\tau)}{\sum_{\forall k}\mathrm{PDP}(k\Delta\tau)}\right)^2}, \tag{16}$$

and the azimuth and elevation spread of arrival and departure are calculated similarly with the power angle profiles.

3.5 Reference Measurements, Calibration, and Verification

Reference measurements for verification and validation have been conducted individually per band and jointly in a multiband configuration.

The purpose of the reference measurements is to compare the measurement results with a known ground-truth in which we can predict the behavior. These reference measurements are conducted in a controlled environment and designed to address the different parameters of the multipath components and the dimensions of the channel sounder: amplitude, delay, angle of arrival and departure, polarization.

According to the experimental set-up, the different parameters can be verified jointly, or separated.

In the following sub-sections, we show in detail the results for the sub-THz band.

3.5.1 Verification Setups

The different setups that have been used during the verification are summarized in Table 4.

Table 4 – List of set-ups of the reference measurements.

Set-up	Description	Parameter to be verified
A	An over-the-air (OTA) device is designed and constructed with two vertical wires to generate two multipath components that are measured simultaneously. See Figure 15a.	• FR calibration • Delay • Polarization
B	The Unit A and B are in LOS and separated at different distances in different steps. See Figure 15c.	• Amplitude • Delay • Polarization
C	The Unit A and B are in LOS at a fixed distance, there is a metal plate located vertical on the side, or in the ground. The channel sounder scans in different angles. See Figure 15d.	• Delay • Polarization • Angle of arrival • Angle of departure
D	The radar cross section of a single vertical wire is measured for different impinging angles and polarizations.	• Polarization

The verification of the FR calibration and the resolution of multipath components in the time-delay domain is carried out with the OTA multipath artifact shown in Figure 15(a) and Figure 15(b). After the FR calibration method is validated, the different experiments are conducted to validate the channel sounder in the other dimensions.

The verification measurement of the amplitude and time-delay of the multipath components is verified with LOS measurements in the anechoic chamber at multiple distances between the Unit A and B (TX – RX), as shown in Figure 15(c).

Time-delay and angles (rotating capabilities, and pointing alignment of the antennas) are verified with the set-up in Figure 15(d). Amplitude in the different polarizations is verified with the set-up in Figure 15(c), and amplitude in the different polarizations, time-delay, and angles are jointly verified with the experiment from Figure 15(d).

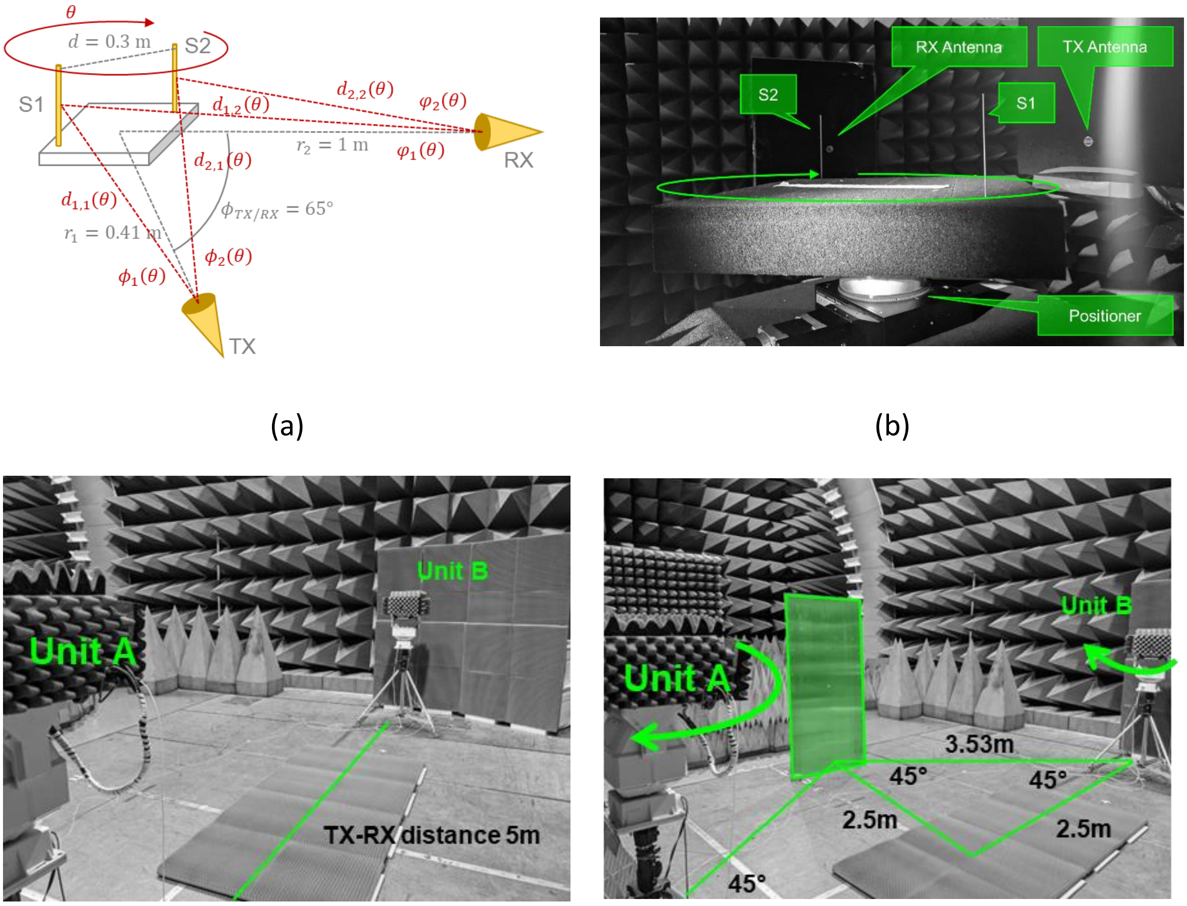

(a) (b)

(c) (d)

Figure 15 – Different set-ups for verification measurements with (a) schematic of the OTA multipath artifact, and (b) picture of it. (c) Path-loss set-up, and (d) multipath from reflection with a vertical metal plate.

3.5.2 FR Calibration and Verification With OTA Multipath Artifact

The analysis of the measurement in the WP3 of 6G BRAINS is based on FFT-processing by searching for peaks to identify multipaths components (or clusters of them, according to the resolution). Therefore, it is important to have a flat spectrum on the measurements to not take artifacts of the measurement system as multipath components.

The FR $\widehat{H}_{\mathrm{OTA}}(f)$ of the complete RF chain at sub-THz (considering antennas) measured in a direct LOS configuration in the anechoic chamber, and its time representation, are displayed in Figure 16, showing multiple peaks that do not correspond to propagation paths, but to artifacts of the measurement system.

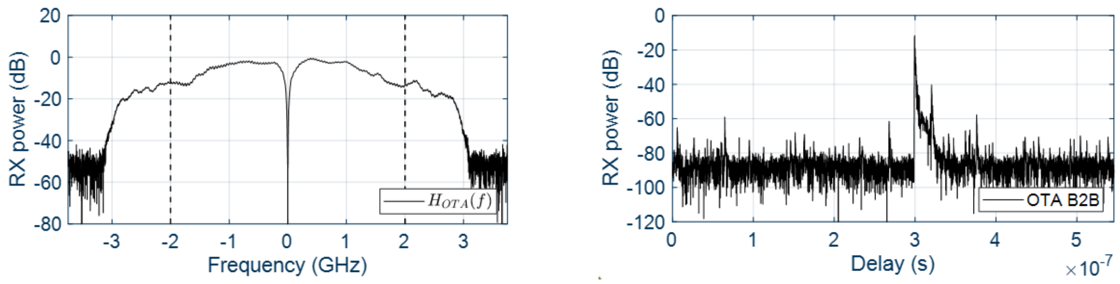

(a) (b)

Figure 16 – OTA back-to-back measurement of the sub-THz sounder (a) FR, and (b) CIR.

The FR calibration is usually performed by equalization in the frequency domain (simplest method is deconvolution carried out in the frequency domain) by dividing the spectrum of the measurements by the spectrum of the complete sounder chain, from a back-to-back connection or OTA back-to-back measurement. The latter, while being preferable by considering the influence of the antenna, requires more effort since it must be carried out in an echo-free environment.

The principal disadvantage of equalization is the enhancement of the measurement noise that results in a SNR degradation. In addition, in our system, the FR has a large notch in the center due to a DC blocker component, which will also enhance noise after equalization.

The equalization process is described in (17),

$$H_{\mathrm{cal}}(f) = \frac{\widehat{H}_{\mathrm{meas}}(f)}{\widehat{H}_{\mathrm{OTA}}(f)} \exp\left(-j2\pi f \frac{d_{\mathrm{ref}}}{c_0}\right) W(f), \tag{17}$$

where d_{ref} is the Unit A to Unit B distance, and the term $\exp\left(-j2\pi f \frac{d_{\mathrm{ref}}}{c_0}\right)$ is used for phase reference calibration (time alignment), and $W(f)$ is the window applied in the frequency domain (in our case Hann window) to reduce sidelobes and ease the path identification process.

Therefore, different methods to minimize the influence of the notch has been tested. One of these methods is the spline interpolation of the center notch in the OTA back-to-back measurement $\widetilde{H}_{\mathrm{OTA}}(f)$ [DSA22], as shown in Figure 17.

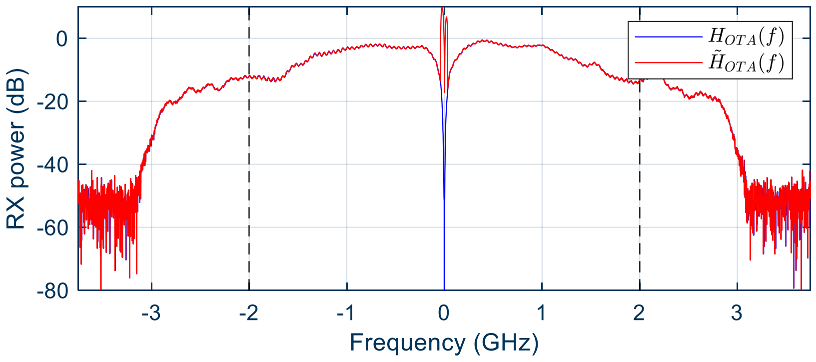

Figure 17 – Raw and interpolated FR of the channel sounder from OTA back-to-back.

The equalization process with the interpolated FR is the same as in (17) but using the interpolated reference measurement $\boldsymbol{\widetilde{H}_{\mathrm{OTA}}(f)}$,

$$\widetilde{H}_{\mathrm{cal}}(f) = \frac{\widehat{H}_{\mathrm{meas}}(f)}{\widetilde{H}_{\mathrm{OTA}}(f)} \exp\left(-j2\pi f \frac{d_{\mathrm{ref}}}{c_0}\right) W(f). \tag{18}$$

An example of the calibration verification using the OTA multipath artifact with two paths at sub-THz is displayed in Figure 18. In the time domain, the raw measured CIR $\hat{h}_{meas}(\tau)$ shows a spread on the two expected paths from the multipath artifact. The calibration result using the raw OTA back-to-back reference measurement $\widehat{H}_{OTA}(f)$ results in an enhanced noise floor in $\hat{h}_{cal}(\tau)$, as shown in Figure 18(b). Finally, the improvements on using the interpolated OTA back-to-back reference measurement $\widetilde{H}_{OTA}(f)$ in (18) are observed in $\tilde{h}_{cal}(\tau)$ in Figure 18(b), visible on a reduction on the noise floor (SNR enhancement) and on a clear possible distinction between the two multipath components.

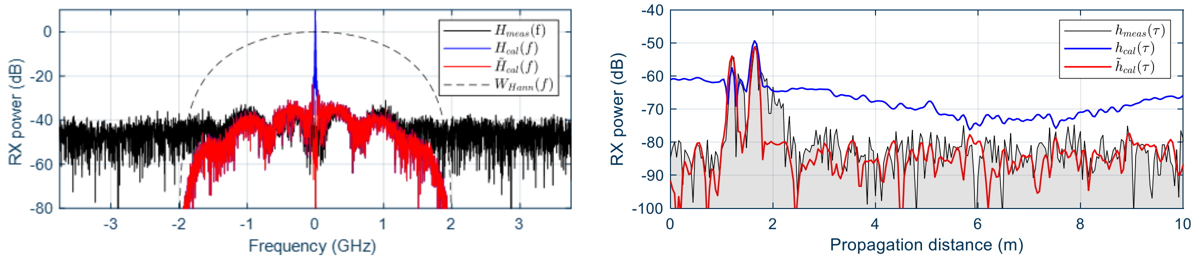

(a) (b)

Figure 18 – Example of the calibration process with the raw OTA back-to-back measurement and the interpolated OTA back-to-back measurement using an OTA multipath artifact (2 paths). (a) FR showing the influence of the notch, and (b) CIR showing the enhance obtained with the interpolated OTA back-to-back measurement.

Finally, the complete process of calibration is verified with the set-up A, shown in Figure 15(a). This OTA artifact allows to jointly estimate all the different geometrical properties of the multipath components as delay, angle of arrival, angle of departure, amplitude, and Doppler. However, in the current configuration of the system, only the time-delay was tested (since neither antenna array was used for the estimation of the directions of arrival and departure, nor continuous movement for Doppler).

The artifact consists of two vertical wires of 1.5 mm diameter (approximately a wavelength at sub-THz). These two wires are located at an arbitrary distance of 30 cm in a platform covered in absorbing material. The TX and RX are located in a fixed and arbitrary bi-static configuration pointing the antennas towards a central point where the artifact is located. The platform is stepwise rotated in 10° angles θ. The different geometrical properties as propagation distance (time-delay) and azimuth of arrival and departure (and amplitude considering the measured antenna pattern) of the two multipath components can be easily calculated and used as the ground-truth, as shown in Figure 19.

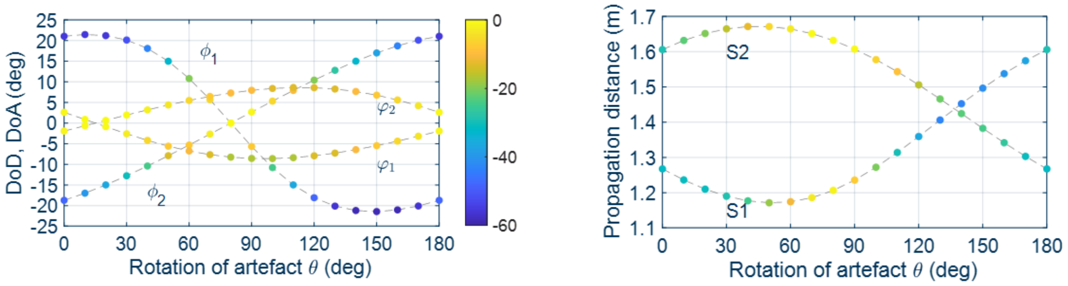

(a) (b)

Figure 19 – Geometrical properties of the multipath in (a) azimuth of arrival and departure, and (b) delay, generated with the OTA multipath artifact

The advantage of this set-up is that generates stressed and relaxed situations in the different domains for different rotation positions θ of the wires, as closely located multipath components in the azimuth of departure at $\theta = 10°$ in Figure 19(a), or in the delay at $\theta = 140°$ as in Figure 19(b). Thus, the capability to resolve multipath components can also be tested.

The results of the measurements are shown in Figure 20. The raw measurements in Figure 20(a) show spurious peaks that can be easily misinterpreted as multipath components, indicating the need of frequency calibration for the analysis. The influence of the notch in the reference spectrum during the calibration process is seen in Figure 20(b). The reduction in SNR after calibration makes that the peak-detector also fails to distinguish between real propagation paths, side-lobes from the calibration, and spurious noisy peaks. Therefore, this calibration method is discarded. Contrarily, the frequency calibration with interpolated notch using (18) shows acceptable results in Figure 20(c), where not only a clean measurement with two clear multipath components can be observed, but also the estimation of the time-delay matches the ground-truth in most of the cases.

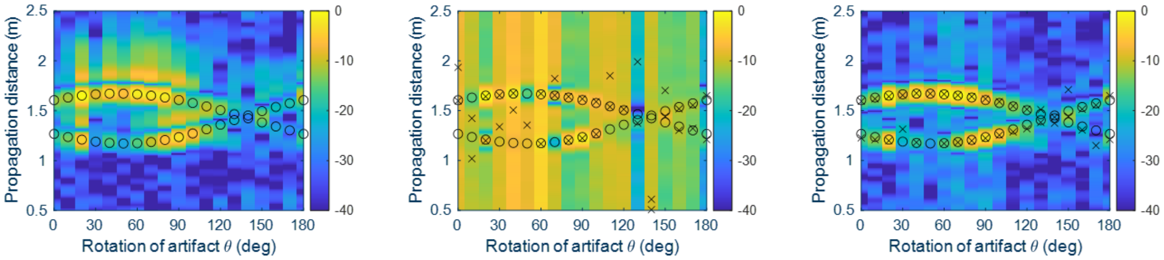

(a) (b) (c)

Figure 20 – Verification results of the FR calibration with OTA multipath artifact. Measurements in the background, ground-truth in circles, and estimated delay with peak-detector in crosses: (a) raw measurement with spurious peaks, (b) calibrated without interpolation of the notch and critical SNR reduction, and (c) calibrated with interpolated notch an enhanced SNR.

3.5.3 Time-Delay and Amplitude of a Single Path Verification

The path-loss measurements verification was conducted in the anechoic chamber using the set-up in Figure 15(c) by separating the Unit A and B on 15 cm steps. The predicted delay of the LOS component (translated into propagation distance) and its amplitude (path-loss), together with the measured CIR for the different polarizations are shown in Figure 21 (five different measurements overlaid). This set-up is appropriate to verify the amplitude since the antennas are aligned and there are no reflection losses or any other mechanism that could introduce variations on the amplitude of the signal. A good match between the prediction and the measurements is observed. The interpolation of the CIR to obtain smooth peaks is done in the frequency domain by FFT interpolation.

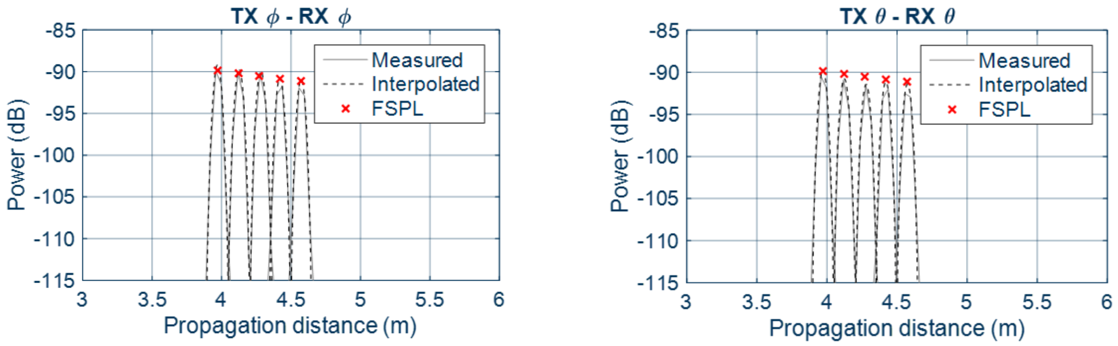

(a) (b)

Figure 21 – Delay and path-loss verification measurements in LOS configuration in the anechoich chamber for (a) horizontal polarization, and (b) vertical polarization.

3.5.4 Multipath Multidimensional Verification

The results of the reference measurements at sub-THz with the vertical plate from Figure 15(b) is shown in Figure 22. The Unit A and B were rotated in 15° steps, covering the LOS component and the reflection on the metal plate. The total power delay profile (by combining the PDP from different angular scans and both polarizations) is displayed in Figure 22(a), showing the expected difference on propagation distance and amplitude of the two MPCs. The power bi-azimuth profile displayed in Figure 22(b) also shows the agreement on the TX and RX angles. Finally, the marginal power azimuth profiles at TX or RX displayed in Figure 22(c) and Figure 22(d) shows the expected results in the azimuth and amplitude of the multi-path components.

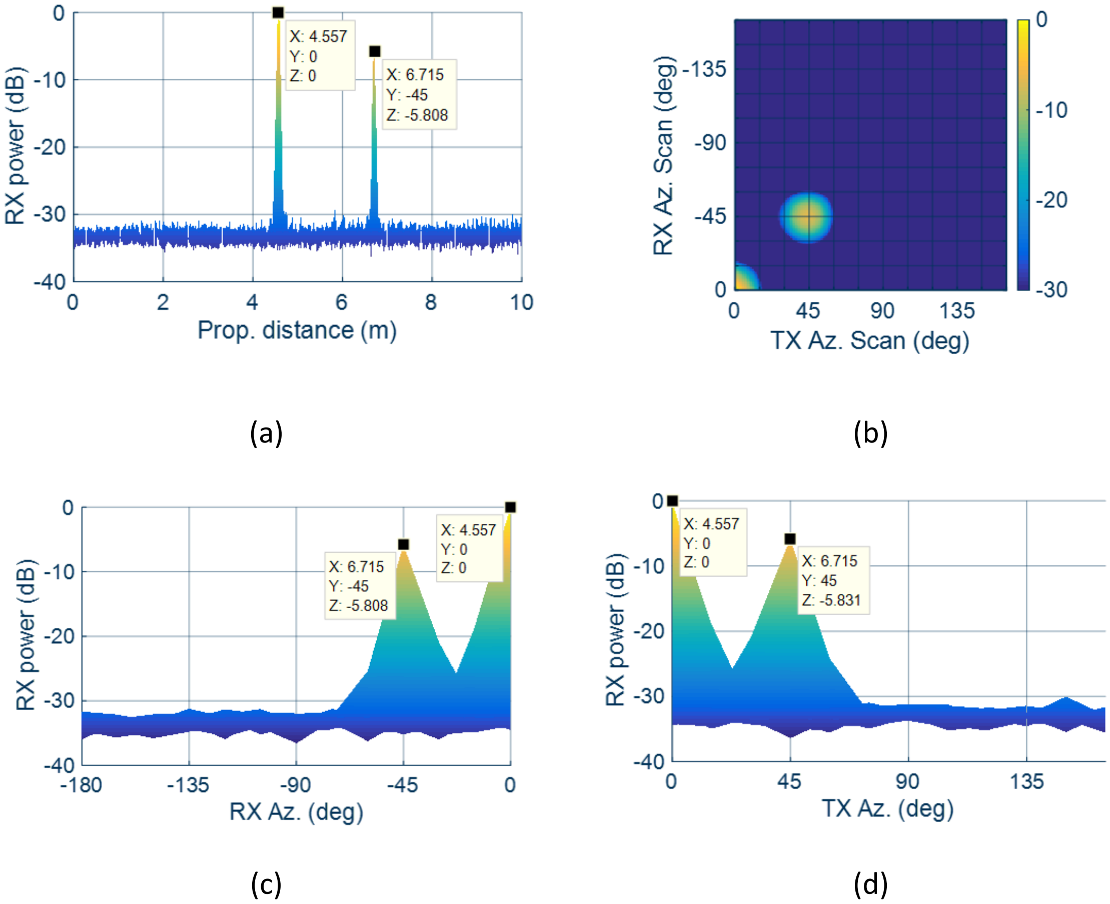

(a) (b)

(c) (d)

Figure 22 – Marginal power profiles from the multidimensional measurements of the multipath artifact with a vertical plate at sub-THz. (a) Power delay profile, (b) power bi-azimuth profile, (c) power azimuth profile at the RX, and (d) power azimuth profile at the TX.

3.5.5 Verification of Polarization

The capability of the channel sounder to measure the polarization of the multipath components has been verified using interferometry by combining the different multipath components from the set-up in Figure 15(c) and Figure 15(d).

The equivalent base-band FR of the dual-polarized channel considering isotropic radiators can be represented as,

$$\mathbf{H}(f) = \sum_{l} \alpha_l \underbrace{\begin{bmatrix} \gamma^{\phi\phi} & \gamma^{\theta\phi} \\ \gamma^{\phi\theta} & \gamma^{\theta\theta} \end{bmatrix}}_{\boldsymbol{\Gamma}_l} \exp(-2\pi j\, f\, \tau_l), \tag{19}$$

where α_l and τ_l are the path-loss and delay of the l^{th} path, respectively, and $\boldsymbol{\Gamma}_l$ is the complex reflection coefficient for the different polarizations. In the LOS case,

$$\boldsymbol{\Gamma}_{\text{LOS}} = \begin{bmatrix} 1 & 0 \\ 0 & 1 \end{bmatrix}, \tag{20}$$

and after scattering (considering a single order specular reflection and no cross-polarization)

$$\mathbf{\Gamma}_{\mathrm{V/H}} = \begin{bmatrix} r_{p/s} & 0 \\ 0 & r_{s/p} \end{bmatrix}, \tag{21}$$

depending on if the reflection surface is vertical *V* or horizontal *H*, and where $r_{p/s}$ are the reflection coefficient for a vertically or horizontally polarized (relative to the reflection plane) impinging wave.

The reflection coefficients can be calculated from Fresnel's equation:

$$\begin{aligned} r_s &= \frac{n_i\, cos(\phi_i) - n_t\, cos(\phi_t)}{n_i\, cos(\phi_i) + n_t\, cos(\phi_t)}, \\ r_p &= \frac{n_t \cos(\phi_i) - n_i \cos(\phi_t)}{n_t \cos(\phi_i) + n_i \cos(\phi_t)}, \end{aligned} \tag{22}$$

where the transmitted angle $\phi_t = \operatorname{asin}\left(\sin(\phi_i)\frac{n_i}{n_t}\right)$ is calculated from Snell's law.

An example of the reflection coefficient for different impinging angles is show in Figure 23(a). The amplitude (and phase) of the reflected wave depends not only on the impinging angle, but also on the polarization of the impinging wave, and the orientation of the interface plane. A vertically polarized wave incident to a vertical plane as a wall, will be reflected with more power and with a change on the phase compared to a horizontally polarized impinging wave, as shown in Figure 23(b). The opposite happens when the reflecting surface is a horizontal plane (e.g., a ground reflection), as displayed in the schematic in Figure 23(c).

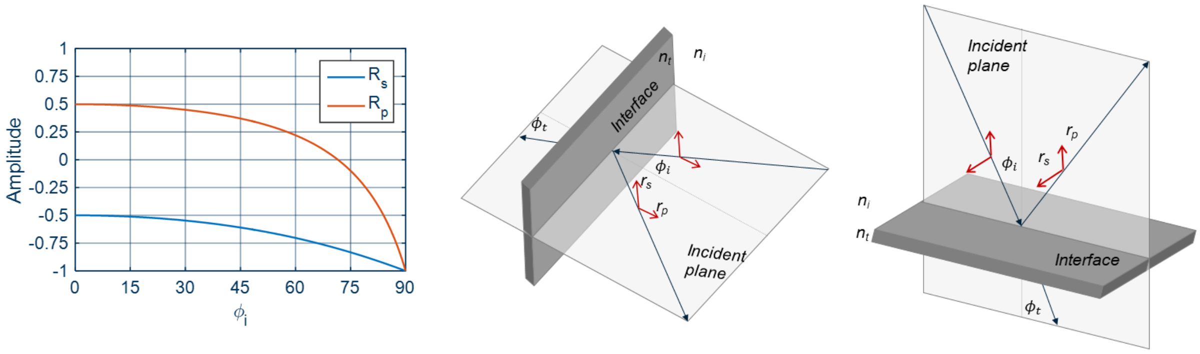

(a) (b) (c)

Figure 23 – (a) Example of reflection coefficients for different impinging angles and polarization. (b) and (c) show the relation between the reflection coefficient and the orientation of the reflecting interface.

Three different set-ups have been used to test the accuracy and verify the capability of the channel sounder on measuring the polarization of the multipath components. Figure 24(a) shows the combination of two direct paths obtained by measuring two different positions of the Unit A and B. Figure 24(b) and Figure 24(c) show the case of a single Unit A and B positions, but two different angular scans, towards the vertical metal plate located standing and towards the metal plate located on the floor, respectively.

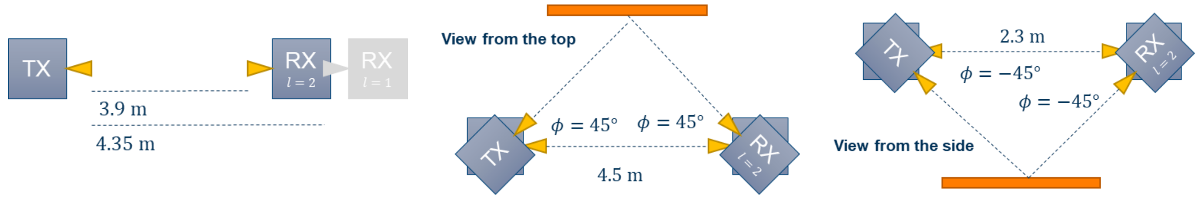

(a) (b) (c)

Figure 24 – Different experiments combining multipath components for analysis of the interferometry pattern.

The interferometry pattern is calculated as the summation of the two different multipath components in the complex domain,

$$\begin{aligned}\mathbf{H}(f) &= \sum_{l=1,2} \alpha_l\, \mathbf{\Gamma}_l \exp(-2\pi j\, f\, \tau_l)\,, \\ &= \alpha_1\ \mathbf{\Gamma}_1 \exp(-2\pi j\, f\, \tau_1) + \alpha_2\ \mathbf{\Gamma}_2 \exp(-2\pi j\, f\, \tau_2).\end{aligned} \tag{23}$$

Since the measurements are conducted in a single horizontal or vertical plane, we concentrate on the co-polarized elements,

$$\begin{aligned}H^{\phi\phi}(f) &= \alpha_1\gamma_{1,1,1} \exp(-2\pi j\, f\, \tau_1) + \alpha_2\gamma_{1,1,2} \exp(-2\pi j\, f\, \tau_2) \\ H^{\theta\theta}(f) &= \alpha_1\gamma_{2,2,1} \exp(-2\pi j\, f\, \tau_1) + \alpha_2\gamma_{2,2,2} \exp(-2\pi j\, f\, \tau_2)\end{aligned} \tag{24}$$

While (18) allows a joint verification of $\alpha_l, r_{s/p}, \tau_l$, a very particular case can be analyzed at $f = 0$:

$$\begin{aligned}H^{\phi\phi}(f = 0) &= \alpha_1\gamma_{1,1,1} + \alpha_2\gamma_{1,1,2} \\ H^{\theta\theta}(f = 0) &= \alpha_1\gamma_{2,2,1} + \alpha_2\gamma_{2,2,2},\end{aligned} \tag{25}$$

where a constructive or destructive interference (independently of the parameters α_l and τ_l) shows the polarization dependent phase change after reflection.

3.5.5.1 Verification of Polarization With Direct Paths

In this case, two different LOS paths are combined in the complex domain. Both paths correspond to two different measurements in LOS separated 45 cm, as shown in Figure 24(a).

The interferometry pattern of the co-polarized components in horizontal polarization $H^{\phi\phi}(f = 0)$ and vertical polarization $H^{\theta\theta}(f = 0)$ from two direct paths with a scattering matrix as displayed in (20) (eye matrix) is

$$\begin{aligned}H^{\phi\phi}(f = 0) &= \alpha_1 + a_2 \\ H^{\theta\theta}(f = 0) &= \alpha_1 + a_2\end{aligned} \tag{26}$$

showing that in both polarizations there is constructive interference, and the amplitude is the same. The simulated and measured interferometry pattern for all the frequencies are shown in Figure 25.

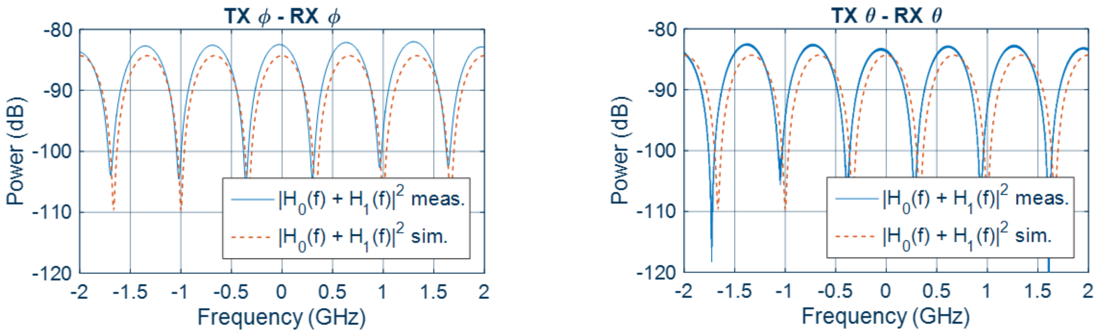

(a) (b)

Figure 25 – Interference pattern for two direct paths for (a) horizontal polarization and (b) vertical polarization.

3.5.5.2 Verification of Polarization From Direct Path and Reflection

In the first case, the reflection is captured from the vertical plate shown in Figure 15(b) and combined with the LOS component. These two paths were taken from two different scans in the angular domain for the same position of the Unit A and B, one into the LOS direction, and the second into the metal plate. The interfering pattern at $f = 0$ results in

$$H^{\phi\phi}(f = 0) = \alpha_1 + a_2 r_p$$
$$H^{\theta\theta}(f = 0) = \alpha_1 - a_2 r_s \tag{27}$$

where there is a constructive interference (peak) in the horizontal polarization and a destructive (valley) in the vertical, as shown in Figure 26.

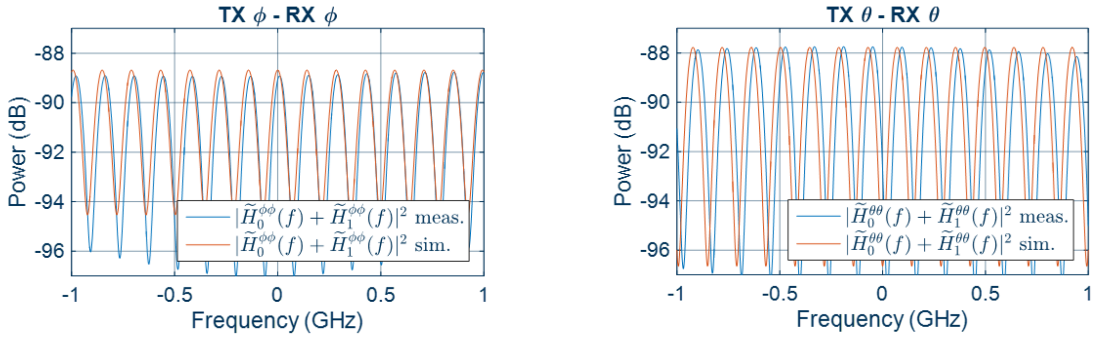

(a) (b)

Figure 26 – Interference pattern for a direct path and a reflection from a vertical surface for (a) horizontal polarization and (b) vertical polarization.

On the other hand, with a reflection on a horizontal surface, the results show the contrary, where the interfering pattern at $f = 0$ is

$$\begin{aligned} H^{\phi\phi}(f=0) &= \alpha_1 - a_2 r_s \\ H^{\theta\theta}(f=0) &= \alpha_1 + a_2 r_p \end{aligned} \tag{28}$$

showing the destructive interference at $f = 0$ (valley) in the horizontal polarization and the constructive (peak) in the vertical polarization, as seen in Figure 27.

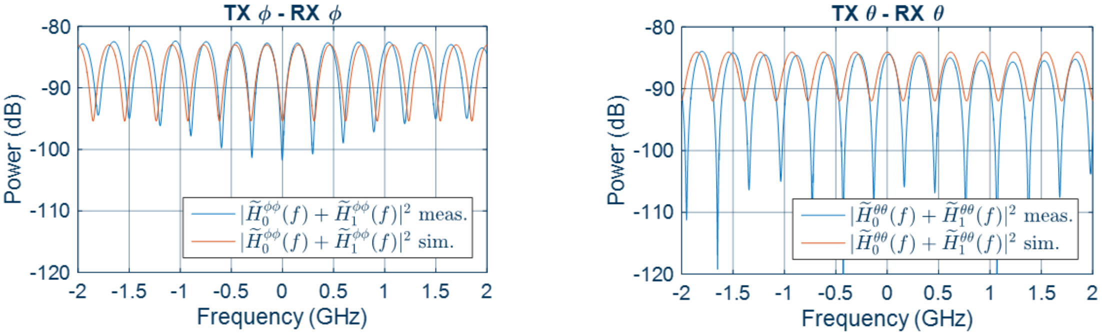

(a) (b)

Figure 27 – Interference pattern for a direct path and a reflection from a horizontal surface for (a) horizontal polarization and (b) vertical polarization.

4 Assembled Quad-Band RF and OWC Channel Sounder

4.1 Specifications

The quad-band RF and OWC channel sounder integrates the OWC chain into the previously described RF channel sounder, as shown in the simplified schematic in Figure 28. The integration between the RF and OWC is in the control and synchronization plane, operating at RF independently from each other. A sketch of the quad-band sounder unit A and B with the antennas and positioners is shown in Figure 29.

The OWC front-ends are connected to RedPitayas© SignalLab 250-12 boards that act as a signal generator in the Unit A and as digitizer in the Unit B.

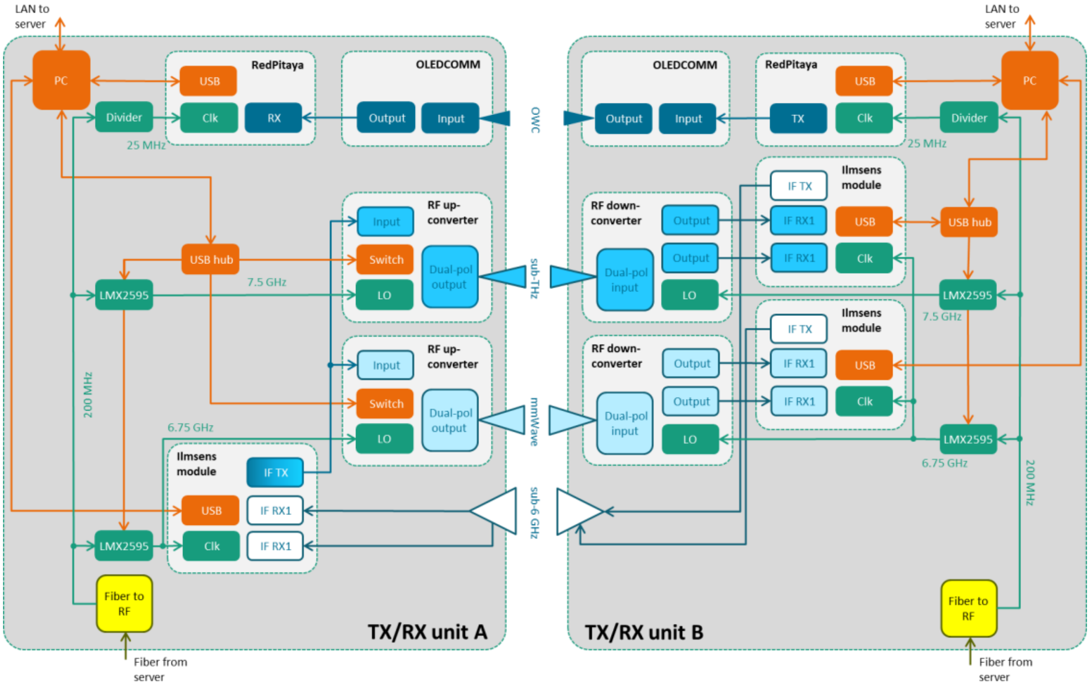

Figure 28 – Schematic of the quad-band channel sounder and the different planes.

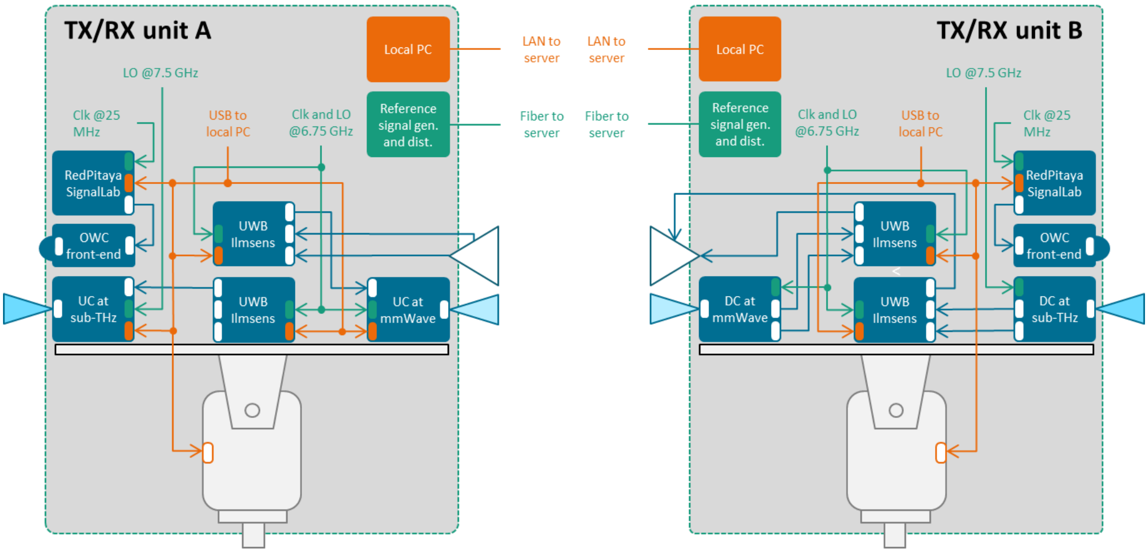

Figure 29 – Simplified schematic of the position of the antennas and UWB devices in the azimuth and elevation positioners.

The OWC is based on the Hamamatsu© S6968 Serie Si PIN PD [HAM22]. The directivity of the PD is shown in Figure 30. The relative sensitivity drops 50% at approximately 30°, which results in a HPBW of approximately 60°.

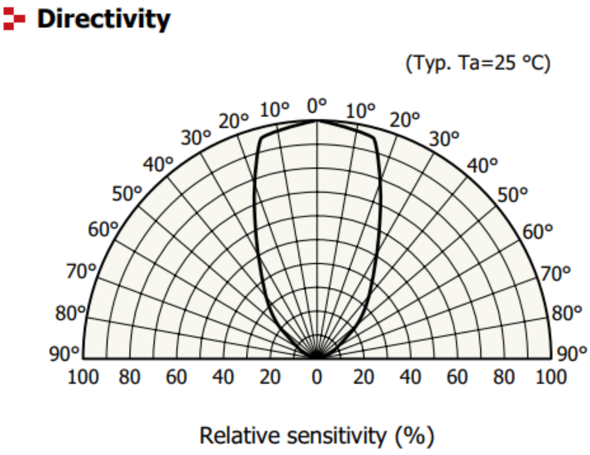

Figure 30 – Directivity of the PD (from datasheet [HAM22]).

4.2 Processing of the Measurements

The excitation signal programmed in the Red Pitaya in Unit B is a multi-sinus with optimized phases (Newman) to minimize non-linearities.

The baseband time representation of the excitation signal is

$$x(n) = \Re\left\{\frac{1}{K}\sum_{k=1}^{K} a_k \exp(j\theta_k)\exp\left(j2\pi f k\frac{B}{K}n\ \right)\right\}, \tag{29}$$

where the phase of each sub-carrier is calculated as $\theta_k = \frac{\pi}{K}(k-1)^2$ with $k = \{1, \ldots, K\}$ and $K = 2^{10}$ sub-carriers, $B = 50 \cdot 10^6$ Hz is the bandwidth of the excitation signal, and $n = \left\{0, \ldots, \frac{N-1}{B_{clk}}\right\}$ s are the time samples with the sampling bandwidth of $B_{clk} = 250 \cdot 10^6$ Hz.

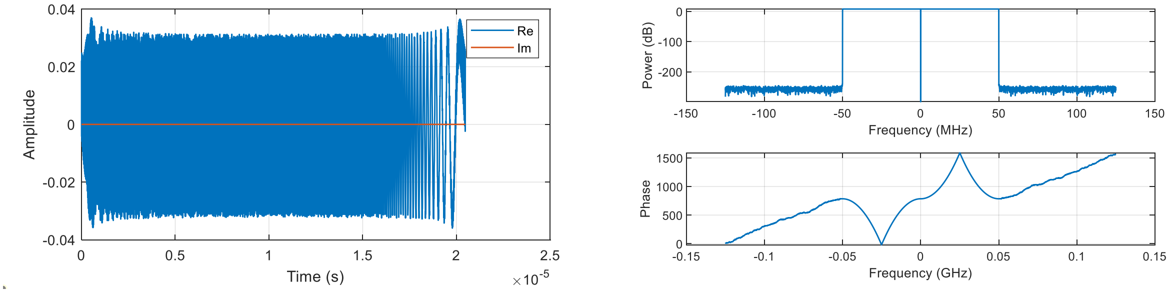

(a) (b)

Figure 31 – Sounding excitation signal for OWC in the quadband channel sounder (a) in the time domain, and (b) spectrum.

The received signal in the OWC band can be represented in the frequency domain as

$$Y(f) = H(f)H_{sys}(f)X(f) + \eta(f), \tag{30}$$

where $H(f)$ is the frequency spectrum of the channel, $H_{sys}(f)$ is the combined FR of the system at the TX and RX (including electronic impairments and effects of the lens, see Section 2.3), and $\eta(f)$ is additive white Gaussian noise. The CIR is recovered as

$$\begin{aligned} \widehat{H}(f) &= Y(f)X^*(f) \\ &= H(f)H_{sys}(f)\underbrace{X(f)X^*(f)}_{=1\forall f\left\{-\frac{B}{2},\frac{B}{2}\right\}} + \eta(f)X^*(f) \\ &= H(f)H_{sys}(f) + \hat{\eta}(f) \end{aligned} \tag{31}$$

The effects of the system can be minimized by conducting a reference measurement in LOS (with the assumption of a single path and therefore a flat spectrum) and equalizing the spectrum of the measured signal (neglecting the noise terms for simplification):

$$\begin{aligned} \widetilde{H}_{cal}(f) &= \frac{Y(f)Y_{ref}^*(f)}{\left|Y_{ref}(f)\right|^2}, \\ &= \frac{H(f)H_{ref}^*(f)\overbrace{H_{sys}(f)H_{sys}^*(f)}^{\left|H_{sys}(f)\right|^2}\overbrace{X(f)X^*(f)}^{1\forall f\left\{-\frac{B}{2},\frac{B}{2}\right\}}}{\left|H_{ref}(f)H_{sys}(f)X(f)\right|^2}, \\ &= \frac{H(f)H_{ref}^*(f)\left|H_{sys}(f)\right|^2}{\left|H_{ref}(f)\right|^2\left|H_{sys}(f)\right|^2\underbrace{|X(f)|^2}_{1\forall f\left\{-\frac{B}{2},\frac{B}{2}\right\}}}, \\ &= \frac{H(f)}{\underbrace{H_{ref}(f)}_{\approx 1\forall f\left\{-\frac{B}{2},\frac{B}{2}\right\}}}. \end{aligned} \tag{32}$$

The measured CIR is then calculated as the inverse FFT of $\widetilde{H}_{cal}(f)$,

$$\hat{h}_{cal}(n) = \sum_{l} P_l \delta(n - \tau_l) \tag{33}$$

where in the OWC case, P_l is the received optical power and τ_l is the delay of the l^{th}path.

Since the amplitude of the path is proportional to the TX power, we expect to have a RX power which will be proportional to the square of the TX power, showing a higher path-loss attenuation than conventional channels [KB97], as displayed in Figure 33(b).

4.3 Reference Measurements

4.3.1 Dynamic Range and Path-loss

In this set-up, the TX – RX unit A and B are located in direct LOS as shown in Figure 32. Different measurements are taken while the unit A is moved away from the unit B from 1 m to 10 m in 1 m steps. The dynamic range is calculated at a TX – RX distance of 5 m as the difference between the peak of the LOS component and the estimated noise floor, [DMT21], as displayed in Figure 33(a). The peak of the LOS path is compared to the theoretical path-loss, showing a very good match in Figure 33(b).

Figure 32 – Path-loss reference measurement scenario for OWC.

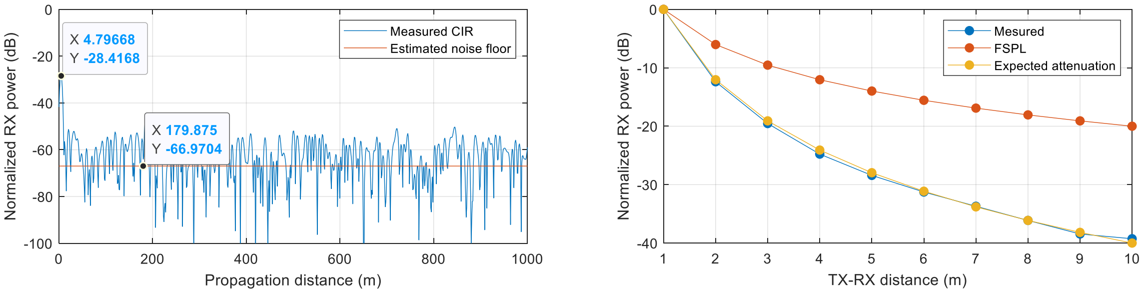

(a) (b)

Figure 33 – (a) Reference measurement of the CIR in LOS at OWC with a TX – RX distance of 5 m, (b) attenuation of the LOS path compared to the free-space path-loss for different TX – RX distance.

5 Expected Test Scenarios

The project intends to verify the theoretical results by applying the invented techniques in scenarios very close to real environmental conditions.

5.1 Multiband Characterization of Propagation in Industrial Scenario

Multiband measurements are planned to be conducted in the production line in the industrial hall at Bosch with the objective of characterizing propagation from empirical measurements at different frequencies using co-located RF and OWC interfaces.

Previous multiband (sub-6GHz and mmWave at 30 GHz and 60 GHz) measurements have been already conducted in the same scenario [DNE22], but using a different set-up, with the aim of calibrating and validating the RT model obtained from point-cloud measurements in this scenario [6GB31, NDV22]. In such a case, the TX was located in an elevation emulating an access point above clutter level and the RXs were located at approximately 1.3 m height emulating user equipment. Since the aim of these measurements was to collect as many measurement positions as possible for statistical analysis and covering the larger possible area within a limited measurement time, omni-directional antennas were used at the RX to save measurement time.

The objective now is to include the sub-THz and OWC radio interfaces. Therefore, since the measurement range is reduced, highly directive antennas (15° HPBW) are employed at both sides of the link at mmWave and sub-THz, increasing the resolution of the channel measurements. This is also more time consuming, and a fewer number of measurement points can be achieved in the limited available time in the scenario. The scenarios are presented below.

5.2 Overview of Scenarios

5.2.1 Path-loss between production lines

In this scenario, the unit A and B are located in between two production lines at the same height. The first set-up consists of path-loss measurements in between production lines by displacing the unit A away from unit B, as shown in Figure 34(a).

5.2.2 Double-side 3D measurements between production lines

A different set-up consists of selecting a fixed unit A and unit B position in LOS and scanning the azimuth domain at both sides of the link, as schematized in Figure 34c.

Finally, unit A is displaced around a corner to generate a NLOS situation. Again, the azimuth domain is scanned at both sides looking for possible reflections that enable communications in NLOS.

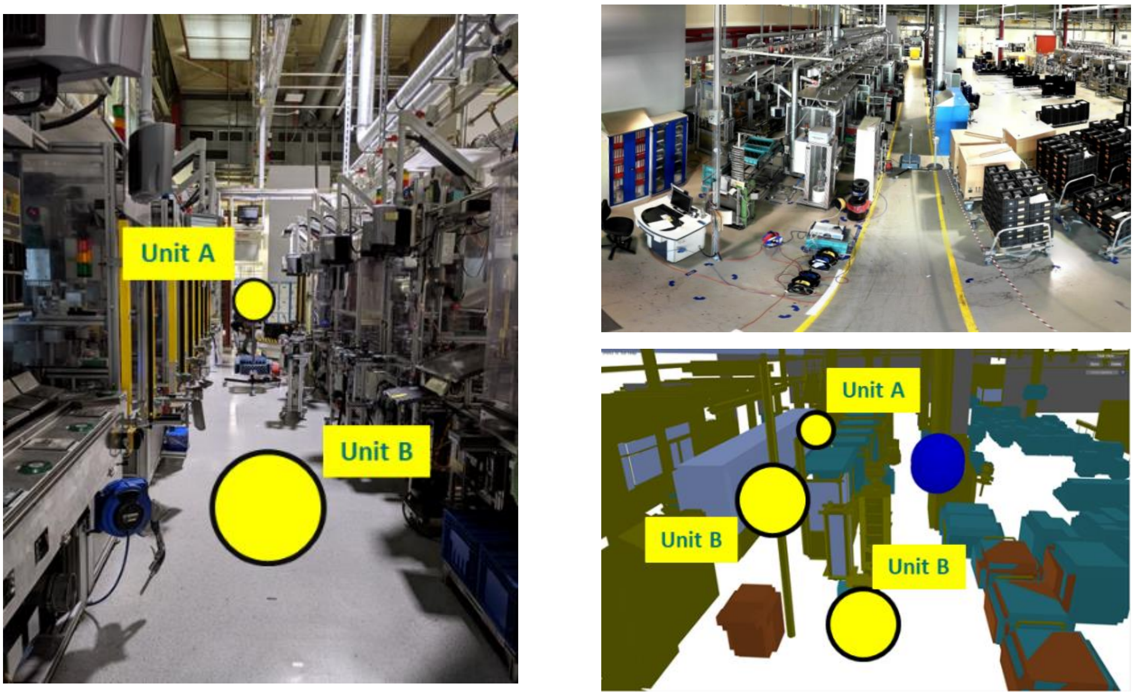

(a) (b)

Figure 34 – (a) Path-loss measurements between production lines, (b) picture of the scenario and 3D model of the scenario with the location of the units for the LOS and NLOS measurements.

6 Summary and Concluding Remarks

This deliverable details the architecture, design and characterization of the fundamental elements of the multi-band (i.e. sub-6 GHz, mmWave, sub-THz, OWC) channel sounder developed in the framework of the 6G BRAINS project for the validation and calibration of the RT channel model developed previously [6GB31].

This channel sounder is actually composed of two independent channel sounder integrated in the same equipment to perform channel measurements on all these four bands:

- The first channel sounder operates simultaneously on the sub-6 GHz (center frequency of 6.75 GHz), mmWave (center frequency of 74.25 GHz) and sub-THz (center frequency of 186.75 GHz) bands. For this purpose, a unified architecture has been developed: a single M-sequence excitation signal with a post-calibration bandwidth of 4 GHz is generated by an unique baseband, then different IF up/down converters allow transposition from/to the three frequency bands mentioned above (see Sections 3.2 and 3.3). The TX and RX signals are then processed according to a detailed process in order to extract the CIR and the spreads of the three channels of interest (see Section 3.4). This first channel sounder has been extensively tested in four scenarios to verify the calibration of the FR, the delay, the polarization and the start and end angle values it provides (see Section 3.5).
- The second channel sounder operates only in the NIR optical band (peak wavelength of 940 nm) and consists of an analog OWC transceiver coupled to a RedPitayas© SignalLab 250-12 signal generation platform. In transmission, the OWC transceiver is based on a single LED with variable directivity (HPBW of 45° or 10°) according to the needs, but respecting in all cases the eye safety standards. On the receiving side, four PDs coupled with focusing lenses are used to optimize the optical power collected and thus the quality of the received signal, allowing the developed OWC RX to surpass existing photoreceptors on the market in terms of 'collection power' (see Section 2.2). The opto-electronic characterization of the OWC transceiver thus obtained shows that the modulation bandwidth at 3 dB and 6 dB are respectively 36 MHz and 47.5 MHz. The RedPitayas© SignalLab 250-12 platform generates on its side a multi-sine signal with a bandwidth after calibration of 50 MHz, which once received after free space propagation is processed to extract the CIR and path loss of the optical propagation channel (see Sections 4.1 to 4.3).

Both channel sounders are in practice assembled in a head with programmable orientation in order to perform tests in real environments (see Section 4.1). Some of the test environments envisaged for the continuation of the WP3 work are finally presented (see Section 5). The tests which will be carried out there will then be the subject of the deliverable project D3.3.

References

[6GB21] 6G BRAINS consortium 2021, https://5g-ppp.eu/6g-brains/ (last access June 2022).

[6GB31] 6G BRAINS, "Deliverable D3.1: 3D Laser measurement of one factory at Bosch with 3D cloud scanner and 3D hand scanner," *online* www.zenodo.org/record/5786456 2021, (last access June 2022).

[AWZ18] A. Al-Kinani, C. -X. Wang, L. Zhou and W. Zhang, "Optical Wireless Communication Channel Measurements and Models," *in IEEE Communications Surveys & Tutorials*, vol. 20, no. 3, pp. 1939-1962, thirdquarter 2018.

[BCA17] A. Behlouli, P. Combeau and L. Aveneau, "MCMC Methods for Realistic Indoor Wireless Optical Channels Simulation," *in Journal of Lightwave Technology*, vol. 35, no. 9, pp. 1575-1587, May 2017.

[BKK93] J. R. Barry, J. M. Kahn, W. J. Krause, E. A. Lee and D. G. Messerschmitt, "Simulation of multipath impulse response for indoor wireless optical channels," *in IEEE Journal on Selected Areas in Communications*, vol. 11, no. 3, pp. 367-379, April 1993.

[BSH18] P. Wilke Berenguer *et al.*, "Optical Wireless MIMO Experiments in an Industrial Environment," *in IEEE Journal on Selected Areas in Communications*, vol. 36, no. 1, pp. 185-193, Jan. 2018.

[CK02] J. B. Carruthers and P. Kannan, "Iterative site-based modeling for wireless infrared channels," *in IEEE Transactions on Antennas and Propagation*, vol. 50, no. 5, pp. 759-765, May 2002, doi: 10.1109/TAP.2002.1011244.

[CZK14] M. I. S. Chowdhury, W. Zhang and M. Kavehrad, "Combined Deterministic and Modified Monte Carlo Method for Calculating Impulse Responses of Indoor Optical Wireless Channels," *in Journal of Lightwave Technology*, vol. 32, no. 18, pp. 3132-3148, Sept. 2014.

[CZH15] P. Chvojka, S. Zvanovec, P. A. Haigh and Z. Ghassemlooy, "Channel Characteristics of Visible Light Communications Within Dynamic Indoor Environment," *in Journal of Lightwave Technology*, vol. 33, no. 9, pp. 1719-1725, May 2015.

[DFM14] D. Dupleich, F. Fuschini, R. Müller, *et al.*, "Directional characterization of the 60 GHz indoor-office channel," *in XXXIth URSI General Assembly and Scientific Symposium (URSI GASS)*, 2014.

[DFV15] V. Degli-Esposti, F. Fuschini, E. Vitucci, *et al.*, "Polarimetric analysis of mm-wave propagation for advanced beamforming applications," *in 9th European Conference on Antennas and Propagation (EuCAP)*, Lisbon, Portugal, 2015.

[DIS17] D. Dupleich, N. Igbal, C. Schneider, *et al.*, "Investigations on fading scaling with bandwidth and directivity at 60 GHz," *in 11th European Conference on Antennas and Propagation (EUCAP)*, Paris, France, 2017.

[DMS20] D. Dupleich, R. Müller, S. Skoblikov, M. Landmann, G. D. Galdo and R. Thomä, "Characterization of the Propagation Channel in Conference Room Scenario at 190 GHz," *in 14th European Conference on Antennas and Propagation (EuCAP)*, 2020.

[DMT21] D. Dupleich, R. Müller and R. Thomä, "Practical Aspects on the Noise Floor Estimation and Cut-off Margin in Channel Sounding Applications," *in 15th European Conference on Antennas and Propagation (EuCAP)*, 2021, pp. 1-5.

[DNE22] D. Dupleich, H. Niu, A. Ebert, *et al.*, "From Sub-6 GHz to mm-Wave: Simultaneous Multi-band characterization of Propagation from Measurements in Industry Scenarios," *in 16th European Conference on Antennas and Propagation (EuCAP)*, Madrid, Spain, 2022.

[DSA22] D. Dupleich, S. Semper, M. Al-Dabbagh, A. Ebert, T. Kleine-Ostmann, R. Thoma, "Verification of THz Channel Sounder and Delay Estimation with Over-The-Air Multipath Artefact," *in 16th European Conference on Antennas and Propagation (EuCAP)*, Madrid, Spain, 2022.

[GB79] F. R. Gfeller and U. Bapst, "Wireless in-house data communication via diffuse infrared radiation," *in Proceedings of the IEEE*, vol. 67, no. 11, pp. 1474-1486, Nov. 1979.

[HAM22] Hamamatsu©, S6968 Series PIN Photodiode, online https://www.hamamatsu.com/content/dam/hamamatsu-photonics/sites/documents/99_SALES_LIBRARY/ssd/s6801_etc_kpin1046e.pdf (last access June 2022).

[HBK19] D. Humphreys, M. Berekovic, I. Kallfass, *et al.*, "An overview of the Meteracom Project," *in Proc. 43-Nd Meeting of the Wireless World Research Forum (WWRF)*, 2019.

[HYK94] H. Hashemi, G. Yun, M. Kavehrad, F. Behbahani and P. A. Galko, "Indoor propagation measurements at infrared frequencies for wireless local area networks applications," *in IEEE Transactions on Vehicular Technology*, vol. 43, no. 3, pp. 562-576, Aug. 1994.

[IEC06] IEC, "IEC 62471:2006: Photobiological safety of lamps and lamp systems", International Electrotechnical Commission, 2006.

[IEC14] IEC, "IEC 60825-1: Safety of laser products – Part 1: Equipment classification and requirements", International Electrotechnical Commission, 2014.

[IEE22] IEEE P2982 - Millimeter-Wave Channel Sounder Verification (VT/ITS/MMW-CSV), https://sagroups.ieee.org/2982/ (last access June 2022).

[JPN02] V. Jungnickel, V. Pohl, S. Nonnig and C. von Helmolt, "A physical model of the wireless infrared communication channel," i*n IEEE Journal on Selected Areas in Communications*, vol. 20, no. 3, pp. 631-640, April 2002.

[KB97] J. M. Kahn and J. R. Barry, "Wireless infrared communications," *in Proceedings of the IEEE*, vol. 85, no. 2, pp. 265-298, Feb. 1997.

[MHD14] R. Müller, R. Herrmann, D. Dupleich, C. Schneider and R. S. Thomä, "Ultrawideband multichannel sounding for mm-wave," *in 8th European Conference on Antennas and Propagation (EuCAP)*, Lisbon, Portugal, 2014.

[MHD15] R. Müller, S. Häfner, D. Dupleich, *et al.*, "Ultra-Wideband Channel Sounder for Measurements at 70 GHz," *in IEEE 81st Vehicular Technology Conference (VTC Spring)*, 2015

[MHD16] R. Müller, S. Häfner, D. Dupleich, *et al.*, "Simultaneous multi-band channel sounding at mm-Wave frequencies," *in 10th European Conference on Antennas and Propagation (EuCAP)*, Davos, Switzerland, 2016.

[MHH19] S. M. Mana, P. Hellwig, J. Hilt, P. W. Berenguer and V. Jungnickel, "Experiments in Non-Line-of-Sight Li-Fi Channels," *2019 Global LIFI Congress (GLC)*, 2019, pp. 1-6.

[MK96] G. W. Marsh and J. M. Kahn, "Performance evaluation of experimental 50-Mb/s diffuse infrared wireless link using on-off keying with decision-feedback equalization," *in IEEE Transactions on Communications*, vol. 44, no. 11, pp. 1496-1504, Nov. 1996.

[MML11] A. Maltsev, R. Maslennikov, A. Lomyev, A. Sevasytanov, and A. Khoryaev, "Statistical Channel Model for 60 GHz WLAN Systems in Conference Room Environment," *in Radioengineering*, vol. 20, no. 2, June 2011.

[MMM22] mmMagic, "Deliverable D2.2: Measurement Results and Final mmMAGIC Channel Models," *online* www.hobbydocbox.com/Radio/69352004-Deliverable-d2-2-measurement-results-and-final-mmmagic-channel-models.html, 2017 (last access June 2022).

[MU15] F. Miramirkhani and M. Uysal, "Channel Modeling and Characterization for Visible Light Communications," *in IEEE Photonics Journal*, vol. 7, no. 6, pp. 1-16, Dec. 2015, Art no. 7905616.

[NDV22] H. Niu *et al.*, "From 3D Point Cloud Data to Ray-tracing Multi-band Simulations in Industrial Scenario", *in IEEE 95th Vehicular Technology Conference: VTC2022-Spring*, Helsinki, 2022.

[PBB97] R. Pérez-Jiménez, J. U. Berges and M. J. Betancor, "Statistical model for the impulse response on infrared indoor diffuse channels, " *in Electronics Letters*, vol. 33, no. 15, pp. 1298-1300, July 1997.

[PKH20] V. Petrov, T. Kurner and I. Hosako, "IEEE 802.15.3d: First Standardization Efforts for Sub-Terahertz Band Communications toward 6G," *in IEEE Communications Magazine*, vol. 58, no. 11, pp. 28-33, November 2020

[SCH16] H. Schulze, "Frequency-Domain Simulation of the Indoor Wireless Optical Communication Channel," *in IEEE Transactions on Communications*, vol. 64, no. 6, pp. 2551-2562, June 2016.

[ZWH22] X. Zhu, C. -X. Wang, J. Huang, M. Chen and H. Haas, "A Novel 3D Non-Stationary Channel Model for 6G Indoor Visible Light Communication Systems," *in IEEE Transactions on Wireless Communications*.

[end of document]